1 **Resolving sea ice dynamics in the north-western Ross Sea during the last 2.6 ka: from seasonal**

2 **to millennial timescales**

3

4

5 Tesi T[1], Belt S.T.[2], Gariboldi K.[3], Muschitiello F.[4], Smik L. [2], Finocchiaro F.[5], Giglio F. [1], Colizza E. [5],

6 Gazzurra G. [3], Giordano P. [1], Morigi C. [3,6], Capotondi L.[7], Nogarotto A.[8], Köseoğlu D.[2], Di Roberto

7 A.[9], Gallerani A.[7]., Langone L. [1]

8

9 (1) Istituto di Scienze Polari - Consiglio Nazionale delle Ricerche ISP-CNR, Via P. Gobetti 101,

10 40129 Bologna, Italy

11 (2) Biogeochemistry Research Centre, School of Geography, Earth and Environmental Sciences,

12 University of Plymouth, Drake Circus, Plymouth, Devon PL4 8AA, UK

13 (3) Departmento di Scienze della Terra , Università di Pisa, Via Santa Maria, 53, 56126 Pisa, Italy

14 (4) Department of Geography, University of Cambridge, Cambridge, CB2 3EN, UK

15 (5) Dipartimento di Matematica e Geoscienze, Università di Trieste, Via E. Weiss 2, 34127, Trieste,

16 Italy

17 (6) Geological Survey of Denmark and Greenland (GEUS), Øster Voldgade 10, 1350 København,

18 Denmark

19 (7) Istituto di Scienze Marine - Consiglio Nazionale delle Ricerche ISMAR-CNR, Via P. Gobetti 101,

20 40129 Bologna, Italy

21 (8) Campus Scientifico, Università Ca' Foscari Venezia, Via Torino 155, 30172 Venezia Mestre, Italy

22 (9) Istituto Nazionale di Geofisica e Vulcanologia (INGV), Sezione di Pisa, Via della Faggiola 32,

23 56126, Pisa, Italy

24

25

26

27

28

29 **Abstract**

30 Time-series analyses of satellite images reveal that sea ice extent in the Ross Sea has experienced

31 significant changes over the last 40 years, likely triggered by large-scale atmospheric anomalies.

32 However, resolving how sea ice in the Ross Sea has changed over longer timeframes has until now

33 remained more elusive. Here we used a laminated sediment piston core (14.6 m) collected from the

34 Edisto Inlet (Western Ross Sea) to reconstruct fast ice dynamics over the last 2.6 ka. Our goal was to

35 first understand the climate expression of selected well-defined sediment laminae and then use these

36 characteristics for reconstructing past sea ice behaviour across the whole sedimentary sequence. We

37 used the recently established sea ice diatom biomarker proxy $IPSO_{25}$ in combination with diatom

38 census counts and bulk analyses. Analyses performed on a suite of discrete laminae revealed

39 statistically significant differences between dark and light laminae reflecting different depositional

40 conditions. Based on their respective biogeochemical fingerprints, we infer that dark laminae

41 accumulated during sea ice thaws in early summer. Under these conditions, laminae contain relatively

42 high concentrations of $IPSO_{25}$ and display an enriched $\delta^{13}C$ composition for the bulk organic matter

43 (OM). While diatom assemblages in dark laminae are relatively homogenous, as the thaw continues

44 later in the summer, *Corethron pennatum* becomes the dominant diatom species, resulting in the

45 formation of light laminae characterized by low $IPSO_{25}$ concentrations. Since *C. pennatum* can

46 migrate vertically through the water column to uptake nutrients and avoid competition in oligotrophic

47 waters, its high concentration likely reflects stratified and ice-free surface waters typical of late

48 summer.

49 Down-core trends show that the correlation between sediment brightness and geochemical fingerprint

50 (i.e., $IPSO_{25}$ and $\delta^{13}C$) holds throughout the record. Based on the knowledge gained at lamina level,

51 our down-core high-resolution reconstruction shows that the summer fast ice coverage changed

52 dramatically during the late Holocene. Specifically, we conclude that the Edisto inlet experienced

53 regular early summer opening between 2.6 ka, and ca. 0.7 ka, after which, coastal fast ice persisted

54 during summer months and ice-free conditions became less frequent. Comparison with previous

55 regional ice core data suggests that the sudden cooling recorded over the Victoria Land Coast region

56 since 0.7 ka might potentially explain our observation of persistent summer fast ice in the Western

2

57 Ross Sea. Our study has shown that multi-proxy data derived from laminated sediments can provide

58 hitherto unknown detail regarding past summer sea ice dynamics in coastal Antarctic regions.

59

60 **1. Introduction**

61 Since multichannel passive-microwave satellite records began in the late 1970's, it has become evident

62 that Antarctic sea ice extent has exhibited sub-regional patterns. Various mechanisms have been

63 proposed to explain such spatial variability, including the El Niño–Southern Oscillation (Stammerjohn

64 *et al*., 2008), the Interdecadal Pacific Oscillation (Meehl *et al*., 2016), the Amundsen Sea Low (Turner

65 *et al*., 2009), as well as basal melting of Antarctic ice shelves (Bintanja *et al*., 2013). Despite these

66 diverse explanations, the collective picture indicates that Antarctic sea ice distribution is expressed by

67 large-scale climate dynamics; in turn, sea ice regulates fundamental aspects of global climate (*e.g*.

68 thermohaline circulation, ocean-atmosphere heat/gas exchange and radiative properties). However, a

69 survey of the current literature clearly reveals that our knowledge of sea ice-climate interactions in the

70 Southern Ocean essentially relies on the last 40 years of satellite imagery, with longer-term records far

71 more elusive because of the paucity of sea ice archives.

72 In this study, we demonstrate the suitability of laminated sedimentary units for the reconstruction of

73 past sea ice dynamics in Antarctica. Laminated diatom ooze deposits have been documented in

74 different regions of the Antarctic margin, including the Antarctic Peninsula (Bahk et al., 2003; Hjort et

75 al., 1997; Leventer et al., 2002; Maddison et al., 2005), the East Antarctic Margin (Alley et al., 2018;

76 Denis et al., 2006; Maddison et al., 2012; Maddison et al., 2006), and the Ross Sea (Finocchiaro *et al*.,

77 2005; McKay *et al*., 2016). Such laminated records often reflect weak post-depositional reworking,

78 which makes them suitable archives for resolving seasonal and sub-seasonal processes driven by

79 short-lived climate variability. Although the formation of laminated units is dependent on local and

80 regional conditions, collectively, their deposition is generally attributed to spring and summer algal

81 bloom events associated with seasonal sea ice retreat (Abram et al., 2014; Finocchiaro et al., 2005;

82 Leventer et al., 2002; Maddison et al., 2012). As such, analysis of such laminated sediments using

83 appropriate proxy signatures of the respective bloom events has the potential to provide insights into

84 local sea ice dynamics (at least) and any changes to these over time.

85 In this study, we analysed laminated sediments from a piston core collected from the Edisto inlet

86 (Western Ross Sea) (HLF17-1, Fig. 1; Fig. 2) to reconstruct past sea ice variability during the late

87 Holocene (last *ca*. 2.6 ka) via an expanded record characterized by continuous diatom-rich

88 laminations. Since the 1970s, sea ice has increased over the Ross Sea, followed by rapid negative

89 anomalies in recent years (*e.g.* 2016) (Parkinson, 2019; Turner et al., 2017). The reasons behind the

90 strong variability of sea ice in the Southern Ocean is a matter of on-going discussion, although

91 compiled evidence suggests that there are likely multiple factors that collectively involve anomalies in

92 the atmospheric and, consequently, oceanic circulation (Meehl *et al*., 2019). Our study focuses on

93 land-fast ice dynamics, which is a major sea ice type common to Antarctic coastal regions. Sea ice

94 reconstructions have traditionally been based on ecological proxies such as diatom assemblages,

95 whose relative abundance in Antarctic sediments reflects changes in sea surface conditions (Armand et

96 al., 2005; Gersonde and Zielinski, 2000; Leventer, 1998). Over the last decade, sea ice diatom-

97 produced Highly Branched Isoprenoid (HBI) lipids have emerged as novel biomarker proxies for

98 Arctic and Antarctic sea ice (Belt, 2018, 2019; Belt and Müller, 2013; Collins et al., 2013; Massé et

99 al., 2011; Vorrath et al., 2019). For the Southern Ocean, the di-unsaturated HBI termed $IPSO_{25}$ ("Ice

100 Proxy for the Southern Ocean with 25 carbon atoms") has been suggested as a biomarker of land-fast

101 ice. In a preliminary study (Belt *et al*., 2016), it was suggested that this source-specific HBI might

102 trace the occurrence of the sympagic (*i.e*. living within sea ice) diatom *Berkeleya adeliensis*, which

103 flourishes predominantly in the bottom sections of fast ice and within the underlying platelet ice

104 (Riaux-Gobin *et al*., 2013). Otherwise, unlike its close structural counterpart IP_{25} in the Arctic (see

105 Belt, 2018 for a recent review), there have been no in-depth investigations into the relationship

106 between $IPSO_{25}$ distributions and Antarctic sea ice characteristics (*e.g*. sea ice concentration, ice type,

107 presence of polynyas, *etc.*). A relatively small number of Holocene sea ice reconstructions based on

108 $IPSO_{25}$ have assumed a positive relationship between sedimentary $IPSO_{25}$ concentration and sea ice

109 extent in a general sense, an interpretation supported in some cases by diatom assemblage data (Denis

110 et al., 2010; Etourneau et al., 2013; Lamping et al., 2020; Massé et al., 2011). Finally, in a recent pilot

111 study of surface sediments from the West Antarctic Peninsula, Vorrath *et al*. (2019) concluded that a

112 number of different factors likely need to be considered when using $IPSO_{25}$ (and combined biomarker

4

113   indices based on IPSO$_{25}$) for paleo sea ice reconstruction, especially given the complex nature of

114   Antarctic sea ice dynamics. As such, it seems likely that the use of IPSO$_{25}$ as a sea ice proxy needs to

115   be carried out on a context-specific, rather than a generic, basis.

116   This study presents the first high-resolution reconstruction of late-Holocene sea ice dynamics in the

117   Western Ross Sea inferred from IPSO$_{25}$. Among its various attributes, the comparatively time-efficient

118   analysis of IPSO$_{25}$ makes it an ideal tool to be used in high-resolution studies dealing with laminated

119   sequences. However, since IPSO$_{25}$ is still a relatively new proxy (see Belt, 2018 for a review) and the

120   likely need to use it according to the specific sea ice setting (see above), our study also involves the

121   analysis of some diatom assemblages and other complementary biogeochemical and lithological

122   parameters, which include the stable isotopic composition of bulk organic carbon, inorganic elemental

123   composition, and grain size measurements.

124   The overarching objectives of this study were threefold: (i) to investigate the extent to which proxy

125   data obtained from dark and light laminae found in HLF17-1 reflected annual, seasonal or sub-

126   seasonal fast ice dynamics; (ii) to use this information to infer the millennial-scale variability of sea

127   ice in the inner-shelf of the Ross Sea over the last 2.6 ka BP; (iii) to rationalise findings through

128   consideration of other climatic parameters pertinent to the late Holocene.

129

130   **2. Regional setting**

131   Edisto Inlet is small ice-filled elongated NNE-SSW fjord situated behind Cape Hallett, along the

132   Victoria Land Coast in the north-western Ross Sea. The fjord is approximately 15 km long and 4 km

133   wide, with a maximum water depth of approximately 500 m and a sill 400 m deep, which divides the

134   fjord from Moubray Bay to the north. Geophysical data (3.5 kHz sub-bottom profiler) acquired during

135   the 2005 PNRA (National Antarctic Research Program) Italian expedition highlighted that the studied

136   core was collected in a very expanded Holocene sequence characterized by soft biogenic laminated

137   sediments (Fig. 1c).

138

139   **3. Materials and methods**

140   3.1. Sampling and subsampling

141 Piston core HLF17-1 (72° 18.4842' S - 170° 03.2592' E; 465 m water depth) was collected in February

142 2017 in the Edisto inlet on board of the *R/V Italica* (Fig. 1). The core, 14.65 m long, was split into 1-m

143 long sections and stored at 4°C on the vessel. At the same site, a box corer (HLF17-2BC, 56 cm) was

144 retrieved and kept refrigerated under the same conditions as the piston core. In the laboratory, open

145 core sections were analysed using an AVAATECH core scanner for high-resolution image acquisition

146 and XRF analyses (0.5-cm sampling interval). Sediments were sub-sampled throughout every 5 cm at

147 1-2 cm thick intervals ($n=295$), while distinct laminae ($n=34$) were subsampled from section III. All

148 subsamples were frozen and freeze-dried prior to analysis.

149 The HLF17-1 core site was visited previously in 2016 on board the *R/V Italica*, during which time a

150 11.43 m long core (HLF16-1) was retrieved and split into sections as described above. Unfortunately,

151 freezing of the core due to failure of the cooling system resulted in the expansion and loss of

152 sediments from the liner ends. Despite this handling issue, the stratigraphy of remaining sediments

153 was well preserved. HLF17-1 and HLF16-1 were correlated with each other using distinctive

154 lamination patterns (Supplementary Material, Fig. S1). HLF16-1was then sub-sampled (10-cm thick

155 intervals) and wet-sieved to isolate carbonate microfossils for the age-depth model of HLF17-1.

156

157 3.2. Bulk analyses

158 Freeze-dried samples were powdered and homogenized in an agate mortar. Acidified sediments (1.5 M

159 HCl) were analysed using a Thermo Fisher Elemental Analyser (FLASH 2000 CHNS/O) coupled with

160 a Thermo Finnigan Delta plus isotope ratio mass spectrometer (IRMS) for organic carbon (OC, wt.%),

161 total nitrogen (TN, wt.%) and stable carbon isotopes ($\delta^{13}C$, ‰) (D'Angelo et al., 2018; Tesi et al.,

162 2012). Opal content (wt.%) was measured according to the leaching method developed by Mortlock

163 and Froelich (1989). Sediments were placed in Teflon tubes and alkaline dissolution was performed

164 with 0.5 M Na_2CO_3 solution at 80 °C for 5 h. Dissolved silica was measured according to the

165 molybdate-blue spectrophotometric method ($\lambda = 812$ nm). Data are reported as weight percentage

166 (wt.%) of SiO_2 x ($0.4H_2O$).

167 Major (%) and minor (ppm) elements were quantified using a wavelength dispersive Philips PW 1480

168 sequential X-ray fluorescence spectrometer (XRF). Analyses were carried out on pressed powder

169   pellets applying the matrix correction as presented in Dinelli *et al.* (2001). Aliquots designated for

170   XRF were used to make loss-on-ignition (LOI, 950°C) measurements. The reproducibility for major

171   and minor elements was ca. 7% and 5%, respectively, and shifted to ca. 15% for minor elements

172   <10ppm (Dinelli *et al.*, 2001). In this study, only the major lithogenic elements are presented (SiO_2,

173   Al_2O_3, TiO_2, Fe_2O_3 and K_2O; the remaining XRF data can be found in the Supplementary Material).

174   XRF analyses were performed exclusively on light and dark laminae sub-sampled from section III.

175   The grain-size of each bulk sediment sample was determined using a Malvern Mastersizer

176   Hydro2000S Diffraction Laser unit for the <2 mm size fraction. Sand, silt and clay fractions were

177   determined using the grain-size classification proposed by Udden-Wentworth (1922).

178   All bulk data not discussed in detail in the main text are presented in the Supplementary Material.

179

180   3.3 HBIs

181   Sediments were extracted, purified and analysed using the analytical method described previously

182   (Belt *et al.*, 2019). Briefly, prior to extraction, 9-octylheptadec-8-ene (9-OHD; ca. 0.1 µg) was added

183   to sediments as an internal standard to enable quantification of $IPSO_{25}$ by gas chromatography–mass

184   spectrometry (GC–MS). Sediments were subsequently saponified in methanolic KOH (H_2O/MeOH,

185   1:9; 5% *m/v* KOH) for 60 min at 70°C. After extraction with hexane (3 x 3 ml), the centrifuged

186   supernatant containing HBIs was dried under a N_2 stream. The dry extract was re-dissolved in hexane

187   (500 µl) and purified using open column chromatography (SiO_2, 38-63 µm). The eluted hexane

188   fraction (3 x 2 ml) was dried under a N_2 stream and re-dissolved in 300 µl of hexane prior to GC–MS

189   analysis.

190   HBIs were quantified via GC–MS using an Agilent 7820a chromatograph fitted with a J&W DB5-MS

191   column (30 m length, 0.25 mm i.d., 0.25 µm film thickness) coupled to a 5977b Mass Selective

192   Detector (MSD). The oven temperature ramp was programmed from 60°C to 280°C at 10°C/min.

193   During the ramp, the MSD operated in both Selective Ion Monitoring (SIM) and SCAN modes.

194   The sea ice algae-derived biomarker $IPSO_{25}$ (HBI diene II) and a tri-unsaturated HBI made by certain

195   open water diatoms (Belt *et al.*, 2017), referred to here as HBI III, were identified by comparison of

196   their mass spectra with those published in previous studies (Belt, 2018; Belt et al., 2012). The injection

197   of C_8-C_{40} alkanes (Sigma-Aldrich) was used to further check the retention indices of $IPSO_{25}$ and HBI

198   III. Quantification of $IPSO_{25}$ and HBI III (Fig. S2) was achieved by integrating peaks of ions *m/z*

199   348.3 and 346.3, respectively, in SIM mode followed by normalizing to the corresponding peak area

200   of the internal standard (9-OHD) and an instrumental response factor obtained by analysis of a

201   purified standard. Data are presented as ng/g opal since both biomarkers are only produced by diatoms

202   and to circumvent the effect from dilution with lithogenic particles and other sources of OC. For

203   example, other algae common to Antarctica such as *Phaeocystis Antarctica* are within the non-silica

204   (and non-HBI) producing *Prymnesiophyte* class, and may potentially contribute to the total OC

205   (Arrigo et al., 2000; Arrigo and van Dijken, 2004). Normalisation of $IPSO_{25}$ to the opal content thus

206   eliminates such possible types of dilution effect. In any case, we also provide our HBI biomarker data

207   in ng/g OC and ng/g dry sediment in the Supplementary Material (Fig. S3 and S4).

208

209   3.4. Diatom analyses

210   An aliquot of each dry sediment (ca. 0.2 g) was treated in a beaker containing a solution of distilled

211   H_2O (40 ml for each sample), H_2O_2 (60 ml for each sample; concentration 40%) to dissolve organic

212   matter, and $Na_4P_2O_7$ (100 mg) to disaggregate sediment particles. The suspensions were heated (70° C;

213   45 min), followed by the addition of 10 ml of HCl (concentration 10%). Suspensions were then heated

214   (70° C; 15 min) and rinsed repeatedly with distilled water in order to reach a pH of ca. 5–6. Rinsing

215   was performed every 8 hours to allow diatoms to settle. The resulting suspensions were then reduced

216   to a volume of 50 ml. A coverslip was placed inside a petri dish and a known volume of suspended

217   material (ca. 150–300 µL) was pipetted into it, together with distilled water in order to achieve a

218   heterogeneous distribution of diatoms on the surface of the dish. After removing excess water,

219   coverslips were glued to microscope slides using the Norland Optical Adhesive 61 (NOA61) and dried

220   under UV light. At least 300 diatom frustules were counted for each slide following the method

221   proposed by Crosta and Koç (2007), which revised Schrader and Gersonde (1978) and Armand

222   (1997). *Corethron pennatum* was counted as one when more than half a valve was present. The

223   relative abundance of each diatom species in a sample was calculated as the percentage of valves of a

224   given species in relation to the total number of valves counted in each sample. In addition, relative

225   biovolume contribution was calculated following the equation and individual biovolumes proposed for

226   each species by Alley *et al*. (2018).

227

228   3.5. Chronology

229   A detailed description of HLF17-1 chronology is presented in section 4.3. Here, we present the

230   analytical methods used to constrain the different dated horizons encompassed by the age-depth model

231   (Table 1). The top of HLF17-1 core was dated using the short-lived radionuclide ^{210}Pb (maximum

232   penetration depth, Fig. S5). ^{210}Pb activity was derived from its daughter nuclide ^{210}Po via alpha

233   spectrometry, following the procedure presented elsewhere (Frignani et al., 2005). XRF core scanning

234   data (0.5 cm resolution) were used to identify possible cryptotephra layers within the core. A

235   significant anomaly in some element ratios (*i.e.* Zr/Sr and Nb/Sr) was found at 136.5 cm

236   corresponding to a peak in volcanic ash concentration (cryptotephra). The bulk layer was treated in

237   H_2O_2 (40% concentration) to dissolve organic matter and with HCl (10% concentration) to dissolve

238   carbonate. Resulting sediment was impregnated in epoxy resin and the textures and composition of

239   glass particles were studied at the *Istituto Nazionale di Geofisica e Vulcanologia, Sezione di Pisa*

240   (INGV-Pisa) using a scanning electron microscope (SEM), Zeiss EVO MA coupled with Oxford-

241   Aztec Energy EDS Analysis System. Standards of volcanic glass were analysed to test the accuracy of

242   data during the SEM analyses (Fig. S6).

243   Radiocarbon dating of bulk OC (*n*=5) and carbonate samples (*n*=6) was performed via accelerated

244   mass spectrometry (AMS) at The National Ocean Sciences Accelerator Mass Spectrometry (Woods

245   Hole Oceanographic Institution, USA) and at the Poznan Radiocarbon Laboratory (Poland). The

246   Bayesian age-depth model was constructed in R using the Bchron package (Haslett and Parnell, 2008).

247

248   3.6. Statistical analyses

249   T-tests were used to determine whether the populations of dark and light laminae were statistically

250   different from each other at $p < 0.01$ (Excel, Analysis ToolPak). When the variance was different

251   among populations, we ran the test assuming unequal standard deviation. Complete linkage

252   agglomerative hierarchical clustering (AHC) was carried out using IPSO$_{25}$, δ^{13}C (OM), and *C.*

253   *pennatum* (% biovolume) as descriptive variables in order to determine their ability to separate light

254   and dark laminae into distinct groups. Subsequently, the same explanatory variables were used to build

255   a classification tree (CT) model via the Classification and Regression Trees (CART) algorithm of

256   Breiman *et al.* (1984) to determine thresholds that best separated light and dark laminae. Primary and

257   surrogate splits were considered, and the CT was pruned by minimizing classification accuracy after

258   10-fold cross-validation (Fig. S7).

259

260   **4. Results and discussion**

261   This section initially focuses on the origin of dark and light laminae, followed by the reconstruction of

262   centennial-scale fast ice variability in the Edisto inlet throughout the late Holocene.

263

264   **4.1 Dark and light laminae composition**

265   Core HLF17-1 exhibited well-defined dark and light laminae on a mm- to cm-scale throughout the

266   record. In order to understand the origin of laminations and their relationship with sea ice, we sub-

267   sampled individual laminae from section III of core HLF17-1 (*n*=34, Fig. 2) since these were

268   sufficiently thick to be collected without cross-contamination from adjacent sections. Overall, *t*-test

269   analyses of IPSO$_{25}$, geochemical and taxonomic data revealed that dark and light laminae were

270   statistically different from each other with, however, important differences depending on the

271   parameter (Table 2).

272   For example, the mean IPSO$_{25}$ concentration was much higher in the dark laminae compared to the

273   light laminae (Table 2; *p*<0.01) (Fig. 3b). We interpret this as an indication of the opening of the inlet

274   during the summer ice break-up following the spring sympagic bloom, resulting in relatively high

275   IPSO$_{25}$ concentrations in the dark laminae. In contrast, we suggest that lighter sediments with low

276   IPSO$_{25}$ reflect largely (later) ice-free conditions, with lower contributions from sympagic algae.

277   Related inferences were made previously by Massé *et al.* (2011) following analysis of IPSO$_{25}$ in

278   laminated near-surficial sediments from Adélie Land (East Antarctica). Thus, alternating IPSO$_{25}$

279   concentrations were identified in contrasting light/dark laminated sediment sections believed to

10

280   represent varying seasonal input; however, the precise seasonal characteristics of the individual

281   laminae were not confirmed as part of the study by Massé *et al*. (2011) and the relationship between

282   IPSO$_{25}$ concentration and lamina colour/brightness was also not reported.

283   If our interpretations of variable IPSO$_{25}$ in laminated sections from core HLF17-1 are correct, the

284   distribution of diatoms would be expected to follow the lamina colour in line with the IPSO$_{25}$ data.

285   Instead, the *t*-test showed that, with the exception of *Fragilariopsis obliquecostata* ($p<0.01$),

286   differences between dark and light laminae were not statistically significant for the species identified,

287   and the differences observed for *F. obliquecostata* were, in any case, small (Table 2). This contrasts

288   with a qualitative examination of the light laminae, which gave a visual impression of being

289   dominated by *C. pennatum* mats when compared to the dark laminae. Similar observations were made

290   by Alley *et al*. (2018) in laminated sediments collected in Iceberg Alley (East Antarctica). However,

291   Alley *et al*. (2018) also noted that *C. pennatum* is a relatively large diatom, so its abundance, relative

292   to the total number of organisms, can lead to underestimations with respect to biomass or biovolume.

293   Thus, once the relative concentrations of diatoms in core HLF17-1 were re-calculated on a biovolume

294   basis (calculations based on Alley *et al*., 2018, Table 3), *C. pennatum* became the most abundant

295   species in the light laminae (Fig. 3c; Table 3), supporting the visual qualitative examination, and low

296   IPSO$_{25}$ concentrations, as predicted. In fact, since *C. pennatum* can adjust its buoyancy to uptake

297   nutrients beneath the pycnocline, *C. pennatum*-rich sediments likely accumulate towards the end of the

298   summer when surface waters are ice-free, well-stratified and nutrient depleted (Alley et al., 2018;

299   Leventer et al., 2006; Salter et al., 2012), again, consistent with the low IPSO$_{25}$ values. In contrast, for

300   dark laminae, where IPSO$_{25}$ is generally high, the deposition of phyto-detritus is likely associated with

301   the progressive accumulation of sympagic diatoms, as fast ice retreats in early summer, in combination

302   with the first algal blooms, as further evidenced by increases to well-known sea ice associated species

303   such as *F. obliquecostata* and *F. curta* (Table 3).

304   Consistent with this interpretation, the average stable carbon isotopic composition ($\delta^{13}C$) of the OM in

305   the dark laminae was relatively enriched in ^{13}C compared to the light laminae (Table 2; $p<0.01$) (Fig.

306   3d). Indeed, we propose that the isotopic fingerprint of laminae likely reflects the influence of variable

307   sea ice cover on the overall photosynthetic fractionation of CO_2, especially since it is well-known that

11

308   sea ice-derived OM is normally relatively enriched in ^{13}C compared to OM produced in pelagic

309   settings (Massé *et al*., 2011). Under normal CO_2-replete conditions, such as those associated with cold

310   open waters, preferential uptake of $^{12}CO_2$ during photosynthesis leads to isotopically light OM;

311   however, within the confined environment of semi-enclosed sea ice, CO_2 becomes a limiting substrate,

312   with consequential reduction in isotopic fractionation and OM that becomes relatively enriched in ^{13}C

313   (Geilfus *et al*., 2014; Geilfus *et al*., 2015). This effect can be augmented by the formation of melt

314   ponds and percolation of meltwater into the ice matrix during ice brake-up, which can further decrease

315   the dissolved CO_2 concentration (Geilfus *et al*., 2015), while the uptake of "heavy" bicarbonate as an

316   alternative carbon source further increases $\delta^{13}C$ (OM) values (Lehmann *et al.*, 2004).

317   Previous studies have suggested that other factors can also regulate the $\delta^{13}C$ of phytoplankton

318   including nutrient availability, growth rate and morphology (i.e. volume/surface cell ratio) (Crosta et

319   al., 2005; Popp et al., 1999; Popp et al., 1998). While we cannot comment on the quantitative

320   importance of the first two aspects in the current context, we note that some previous in-situ and batch

321   culture studies indicate that the fractionation of ^{13}C during photosynthesis decreases with increasing

322   volume/surface area ratio of the diatom cell (Crosta et al., 2005; Popp et al., 1998). However, in the

323   current study, the most depleted $\delta^{13}C$ values for OM were found in the light laminae dominated by *C.*

324   *pennatum*, which is characterised by a high volume/surface area ratio. Together, these data support our

325   hypothesis that the progressive increase in CO_2 concentration in surface waters upon transitioning

326   from ice-covered to ice-free conditions likely exerted first-order control on the $\delta^{13}C$ signature of

327   diatomaceous OM, with most depleted $\delta^{13}C$ values aligned with light laminae associated with summer

328   pelagic conditions. Conversely, dark laminae contain a higher contribution from ^{13}C-enriched

329   sympagic OM following ice break-up and higher $IPSO_{25}$. Consistent with this, although we did not

330   measure $\delta^{13}C$ for $IPSO_{25}$ in the current study, this biomarker has been previously been shown to be

331   significantly ^{13}C-enriched in both sea ice and sediments ($\delta^{13}C$ = ca. -5 to -18 ‰; Belt *et al.*, 2016, and

332   references cited therein).

333   We note that the diatom *Berkeleya adeliensis* was not observed in any of the laminae analysed, despite

334   the identification of $IPSO_{25}$ in all cases. This might be a result of the occurrence of production of

12

335      $IPSO_{25}$ by other, as yet unidentified, sources; however, HBIs (including $IPSO_{25}$) are only produced by

336   certain diatoms (see Belt, 2018 for a recent review) and none of the other species identified here

337   (Table S1) are known to biosynthesise $IPSO_{25}$. Alternatively, the absence of *B. adeliensis* in all

338   laminae may simply reflect its poor preservation in the water column and in sediments (due to lightly

339   silicified valves) following its release from fast ice, as reported previously (Riaux-Gobin et al., 2011;

340   Tanimura et al., 1990). Indeed, Tanimura *et al.*, (1990) showed that *B. adeliensis* can account for a

341   large fraction of diatom assemblages in sea ice and melt ponds, yet is frequently absent in surface

342   sediments due to dissolution. In addition, we note that some of the *C. pennatum* observed in the

343   current study was present as fragmented frustules. On the other hand, $IPSO_{25}$ appears sufficiently

344   stable in sediments to permit identification in sediments spanning the Quaternary, at least (Belt, 2018,

345   2019).

346

347   The distributions of lithogenic material are also consistent with the biogenic content and associated

348   interpretations of dark and light laminae. Specifically, dark laminae, on average, showed higher

349   concentrations of lithogenic elements, including TiO_2, Al_2O_3 and Fe_2O_3, and K_2O, compared to the

350   light laminae (Table 2; *p*<0.01) (Fig. 3e). Following our interpretations based on $IPSO_{25}$ concentration,

351   diatom assemblages and $\delta^{13}C$ (OM), we suggest that the relatively higher lithogenic content in the dark

352   laminae likely reflects the opening of the inlet, when fast ice thaws and releases mineral dust deposited

353   on sea ice during the preceding months of the year (Atkins and Dunbar, 2009). In fact, according to

354   Atkins and Dunbar (2009), the flux of dust that accumulates over the sea ice in McMurdo Sound (Ross

355   Sea) decreases with increasing distance from the coast and accounts for a large fraction of the total

356   lithogenic particle flux to sediments.

357

358   **4.2 Annual variability and lamination pattern**

359   Overall, our collective biogenic and geochemical proxy data obtained from well-defined laminae

360   suggest that fast ice evolution during summer in the Edisto inlet resulted in the deposition of laminae

361   possessing different colour and composition. Further, by co-plotting the $IPSO_{25}$, $\delta^{13}C$ (OM) and *C.*

362   *pennatum* (% biovolume) datasets (Fig. 4), the two proposed dominant fast ice patterns can be

363   visualized and summarized as follows. At the beginning of summer, the progressive opening of the

364   inlet takes place, leading to the accumulation of dark laminae characterized by high IPSO$_{25}$, enriched

365   δ^{13}C (OM) and low *C. pennatum* (% biovolume) (Fig. 4). We infer that the biogenic material that

366   forms these darker laminae has two main sources: (i) sympagic diatoms living within the brine matrix

367   of sea ice, which are subsequently released as the ice thaws, and (ii) diatoms that flourish in surface

368   waters as the inlet opens in summer (e.g. *F. curta*). Further, since satellite images show that the

369   complete opening of the inlet can take a few weeks, we believe that the deposition of sea ice diatoms

370   and sea ice-associated diatoms likely coexist. This is confirmed by the co-occurrence of IPSO$_{25}$ and

371   HBI III in the dark laminae (Fig. S3), the latter being derived from certain pelagic diatoms (*e.g.* (Belt

372   et al., 2017) and commonly found in marginal sea ice zones (Belt *et al.*, 2015; Smik *et al.*, 2016;

373   Vorrath *et al.*, 2019).

374   When protracted opening of the inlet occurs (i.e. ice free conditions), the surface nutrient limitation

375   likely favours diatoms that can uptake nutrients underneath the pycnocline typical of oligotrophic

376   waters which develop towards the end of the summer (Alley *et al.*, 2018). Under these conditions, *C.*

377   *pennatum* dominates, generating light laminae (Fig. 4), possibly in the form of rapidly sinking mats

378   bound together by exopolymer mucus secretions and entangled spines (Alley *et al.*, 2018). Our

379   interpretation would clearly benefit from contemporary in situ studies dealing with the composition

380   (diatoms, biomarkers, etc.) of seasonal sinking particulate material inside Antarctic inlets. To the best

381   of our knowledge, however, sediment traps have been deployed for this kind of setting only for short

382   periods (Thomas *et al.*, 2001), although longer studies in the Southern Ocean have been carried out

383   primarily in deep- and mid-shelf environments (Smith *et al.*, 2000)..

384   Our general description of two discrete sea ice scenarios can be refined further by reference to satellite

385   images of the inlet, which reveal marked inter-annual variability of fast ice conditions in summer. For

386   example, Figure 5 shows satellite images from three years (*i.e.* 2012, 2017, 2018) that clearly describe

387   the full spectrum of proposed ice cover and its transitions. Thus, in 2017, ice break-up took place at

388   the beginning of the summer, followed by protracted opening of the inlet. Under these conditions, we

389   infer the deposition of both dark and light laminae (Fig. 5a). In contrast, in 2012, thawing of fast ice

390   was delayed, and the inlet never completely opened by the end of the summer. In this scenario, it is

391   likely that deposits were dominated by dark laminae due to only partial and ephemeral opening of the

392   inlet (Fig. 5b). Finally, in 2018, fast ice persisted throughout the summer along the coastal region. We

393   envision that these circumstances prevented the accumulation of biogenic material or, alternatively,

394   resulted in only a thin deposit (*i.e.* condensed unit) (Fig. 5c).

395   Overall, satellite images from the Edisto inlet taken over the last decade suggest that fast ice dynamics

396   during summer can sometimes be more complex than a simple sequential accumulation of dark and

397   light laminae, as inferred for 2017. This is confirmed by the laminations patter of HLF17-1 that does

398   not exhibit recurring patterns at multi-year scale (*i.e.* over cm or dm) (Fig. 2), likely reflecting the

399   dynamic annual variability in summer sea ice conditions revealed by satellite images shown herein

400   from 2012, 2017 and 2018.

401

402   **4.3. Local reservoir effect and Bayesian age-depth model**

403   Calibrations of radiocarbon ages obtained from carbon pools that are not in equilibrium with the

404   atmosphere require a correction due to the influence of the reservoir effect (Stuiver and Polach, 1977).

405   In addition to the global mean marine reservoir (R) modelled when using the Marine13 curve (Reimer

406   *et al.*, 2013), a further offset (ΔR) needs to be applied to accommodate local influences. Here, we built

407   our age-depth model using ^{14}C ages derived from both carbonate and organic carbon matrices, with

408   additional dates obtained from excess ^{210}Pb and one tephra horizon. Considering the mixed nature of

409   the radiocarbon tests (i.e. organic and inorganic carbon), we used two different local reservoir

410   corrections prior to calibration. Based on U/Th dating of coral samples trapped by the fringing Ross

411   Sea ice shelf (Hall et al. (2010), the ΔR value of the carbonate matrix (ΔR_{CaCO3}) in the Ross Sea has

412   remained relatively stable ($\Delta R_{CaCO3} = 791\pm121$ yrs) over the last 6,000 years. In our records, carbonate

413   tests included benthic foraminifera, planktonic foraminifera and Ophiuroidea found in core HLF16-1

414   (Table 1), and were correlated with core HLF17-1 using distinct lamination patterns common to both

415   cores (Fig. S1, Supplementary Material). For consistency, only benthic foraminifera were used in the

416   final age model, while additional carbonate samples (planktonic foraminifera and Ophiuroidea) from

417   the same core depths were used to independently test the robustness of our chronology and

15

418   assumptions behind using ΔR_{CaCO3} (Table 1). Following calibration, all carbonate skeletal elements

419   belonging to the same horizon displayed similar calendar ages, confirming that the ΔR_{CaCO3}, in

420   addition to being stable over the late-Holocene (Hall *et al.*, 2010), is also appropriate for diverse

421   calcifying organisms (Table 1).

422   In contrast, the ΔR of the acid insoluble organic fraction (ΔR_{OC}) is poorly constrained in Antarctic

423   sediments and is usually derived empirically by radiocarbon dating of surface bulk sediments and their

424   interpolation (Domack et al., 2001; Licht et al., 1998; Mezgec et al., 2017). In the Edisto inlet, Mezgec

425   et al. (2017) used core-top data (box-corer BAY05-bc21, 0-1 cm) to propose a value of 1580±45 years

426   as a general R_{OC} (global + ΔR). However, using the same approach, the remarkably young ^{14}C age

427   (200±30 yrs BP; Table 1) of the surface sediment from box core HLF17-2BC (0-0.5 cm) collected at

428   the same site as piston core HLF17-1, suggests that our core top likely contained "bomb" ^{14}C, which

429   prevents its use to assess ΔR_{OC}.

430   Given the evident limitations of using surface sediments to estimate the local reservoir effect, we

431   derived the ΔR_{OC} by pairing benthic foraminifera (ultimately used in the age-depth model) with

432   organic carbon from the same horizons, relying on the well-constrained ΔR_{CaCO3}. This alternative

433   approach assumes that the accumulation of foraminifera and the deposition of organic carbon in the

434   same horizons were coeval with negligible post-depositional transport. This allowed us to subtract the

435   ^{14}C age of foraminifera (adjusted for ΔR_{CaCO3}) from the ^{14}C age of the organic fraction to obtain the

436   ΔR_{OC} for each level and its relative uncertainty. The average of the three values gave an estimate of the

437   final mean ΔR_{OC} (1320 ± 135 yrs, 1σ). Additional dates used in the age-depth model include the

438   maximum penetration of excess ^{210}Pb (150±20 yrs before 2017, Fig. S1 and S4; ca. seven half-lives

439   according to Arias-Ortiz *et al.* (2018)) and a tephra layer recently found in the Edisto inlet sediments

440   (Fig. S1 and S5) (Mount Rittmann volcano eruption, (Di Roberto *et al.*, 2019), which has been

441   identified in the Talos Dome core (696 ± 2 yrs BP; ice record) (Narcisi *et al.*, 2012), Taylor Dome core

442   (709 ± 71 yrs BP; ice record) (Hawley *et al.*, 2003) and West Antarctic Ice Sheet (WAIS) Divide cores

443   (687 ± 7 yrs cal BP) (Di Roberto *et al.*, 2019). For our final age-depth model, we used the more precise

444   age assignment derived from the annually-counted portion of the WAIS Divide 2014 chronology.

16

445   Our final Bayesian age-depth model for HLF17-1 was built on seven dates (Table 1; Fig. 6). The age-

446   depth model showed that, since 2.6 ka BP, the relatively stable and high accumulation rate in the inlet

447   (ca. 0.7 cm/yr) was followed by an abrupt decrease around 0.7 ka BP (*ca.* 0.2 cm/yr) (Fig. 6).

448

449   **4.4. Late-Holocene reconstruction of sea-ice dynamics in the Edisto inlet**

450   In order to reconstruct the fast ice dynamics during the late-Holocene, we analysed 295 sediment

451   samples throughout piston core HLF17-1. Following our interpretation about the emplacement of

452   laminated strata (section III), we assumed that the down-core distribution of $IPSO_{25}$ and $\delta^{13}C$ (OM) in

453   bulk sediments co-varied as a function of the relative contribution of light and dark laminae. Since the

454   two types of laminae could be further classified, statistically, into two distinct groups based on AHC

455   and CT analyses (see Section 3), we identified suitable thresholds for $IPSO_{25}$ (0.42 ng/g opal) and $\delta^{13}C$

456   (-27.56‰) to best separate the laminae analysed in section III (Fig. 4) into light and dark groupings

457   (Supplementary Material, Fig. S6). By applying these thresholds to bulk sediments, we obtained two

458   sub-groups of $IPSO_{25}$ and $\delta^{13}C$ (OM) which succinctly represented the two dominant types of fast ice

459   coverage in summer: initial summer break-up and ice-free conditions (dashed lines in Fig. 7a,b). As

460   described previously (Section 2), we expected that the third condition – inlet covered throughout the

461   summer – would not be uniquely characterised in our laminated sequence. Rather, when this occurred,

462   permanent fast ice probably resulted in either a gap in accumulation or a condensed sediment unit.

463   Regardless of this limitation, comparison between the down-core sediment brightness and clustered

464    $IPSO_{25}$ and $\delta^{13}C$ (OM) bulk data revealed a good agreement, especially for $IPSO_{25}$ (Fig. 7a,b). This

465   further confirmed that the correlation between sediment colour and geochemical signature observed in

466   section III (laminae) holds throughout the record.

467   Thus, we propose use of the same $IPSO_{25}$ and $\delta^{13}C$ thresholds (dashed lines Fig. 7a,b) to identify

468   periods throughout the late Holocene when fast ice break-up followed by an ice-free inlet was more

469   frequent (grey shaded areas) relative to periods characterized by partial opening of the inlet (see Fig 5a

470   and 5b, respectively). Using this approach, we identify a significant change in the relative frequency of

471   inlet opening and ice-free waters during the late-Holocene. Specifically, our results suggest that

472   between 2.6 ka BP and 0.7 ka BP the inlet opened regularly during summer, while after 0.7 ka BP,

473   there was an abrupt shift characterized by relatively less frequent ice-free conditions (e.g. Fig. 7a,b). It

474   is worth noting that following the shift in ice conditions at 0.7 ka BP, the sediment accumulation rate

475   of the record decreased abruptly from 0.7 to 0.2 cm/yr. This likely occurred due to the absence (or

476   lower frequency) of light laminae deposition, resulting in relatively thinner sediment strata over

477   summers. Finally, the bulk grain-size exhibited a similar temporal shift, becoming progressively

478   coarser after ca. 1.3 ka BP. This overall trend was expected based on the analysis of dark and light

479   laminae, which also displayed small, but statistically significant differences (Table 2; $p<0.01$),

480   although the reason why dark laminae were coarser is, as yet, unknown. We speculate that this might

481   be attributable to the relatively higher concentration of lithogenic material in the dark laminae (mode

482   of dust ranges between 76 and 129 μm, (Atkins and Dunbar, 2009). Nevertheless, the difference

483   between light and dark laminae is somehow counterintuitive considering that the former are dominated

484   by *C. pennatum,* which, as described before, is considerably larger than other diatoms more abundant

485   in dark laminae. However, since *C. pennatum* was mostly present as fragments, despite its high

486   abundance, it is possible that lithic particles played a major role in the overall grain-size distribution.

487

488   **4.5. Fast ice dynamics over the late-Holocene and climate forcing**

489   In order to understand the origin of the shift in sea ice conditions observed around 0.7 ka BP, we

490   compared our results with the extensive dataset compiled by Stenni *et al.* (2017) within the umbrella

491   of the PAGES Antarctica2k programme. The entire database consists of water stable isotope data

492   (δ^{18}O and δD) from 112 records, which permitted a high-resolution reconstruction of past temperature

493   and relative anomalies (relative to 1900–1990 CE) over the last 2 ka BP for seven climatically distinct

494   regions of Antarctica. The composite temperature anomalies reconstruction (10-yr-binned averages;

495   Fig. 7d) for the Victoria Land Coast region based on ice cores near to HLF17-1 (Fig. 1a) shows a clear

496   and abrupt cooling at 0.7 ka BP, which follows the general long-term cooling over Antarctica that

497   started at ca 1.2 ka BP. Previously, Stenni *et al.* (2017) argued that this hemispheric-scale cooling

498   could have been driven by major volcanic eruptions, in agreement with previous studies (McGregor *et*

499   *al.*, 2015). Although the cause of this cooling over the last two millennia is beyond the scope of the

500 current study, it is worth noting that the land fast ice reconstruction based on our marine record agrees

501 well with the temperature anomalies recorded in the Victoria Land Coast. Thus, we attribute less

502 frequent ice-free conditions since 0.7 ka BP to a colder climate inferred from ice core data (Stenni *et*

503 *al.*, 2017), although we also note that our marine record resolves summer dynamics only, while ice

504 cores provide a year-round signature.

505 We also compared our results with those of Mezgec *et al.* (2017) who analysed Holocene diatom

506 assemblages in cores taken from Cape Hallett and Wood Bay (Ross Sea). Interestingly, their data

507 show a sharp increase in the relative concentration of *F. curta* during the late Holocene, which is

508 consistent with the occurrence of more frequent dark laminae in the current study (Table 2 and 3), thus

509 supporting our interpretation of less protracted opening of the inlet during summers along the coast.

510 Another important factor that can have large-scale implications for fast-ice dynamics over Antarctica

511 is the non-annular response (i.e. dipole) of the Southern Ocean to the Southern Annular Mode (SAM)

512 (Bertler et al., 2018; Lefebvre and Goosse, 2005; Lefebvre et al., 2004). This dipole consists of a

513 different regional response in sea ice, with decreases in the Weddell Sea and around the Antarctic

514 Peninsula, and an increase in the Ross and Amundsen Seas during years with a positive SAM index.

515 Due to a low-pressure anomaly in the Amundsen-Bellingshausen sector during positive SAM years,

516 the Weddell and Bellingshausen Seas are subject to more northerly winds, while the Ross Sea tends to

517 have more southerly winds (Lefebvre *et al.*, 2004), inducing a significant cooling at the surface and an

518 increase in the Ross Sea ice cover (Lefebvre and Goosse, 2005; Lefebvre et al., 2004). However, as far

519 as our data are concerned, comparison between our reconstructed fast ice dynamics and the SAM

520 derived from proxy records over the last 1000 yrs (Fig. 7e) (Abram *et al.*, 2014) does not suggest a

521 direct influence of the latter. In particular, the abrupt shift that characterizes our record around 0.7 ka

522 BP even opposes that expected from a negative SAM (Lefebvre *et al.*, 2004). Likewise, the negative

523 SAM should also have resulted in warmer conditions over the Ross Sea, which does not concur with

524 the sharp cooling reconstructed in the Victoria Land Coast region based on ice core records (Stenni *et*

525 *al.*, 2017) (Fig. 7d).

526 However, stronger westerlies in the region of the Antarctic Circumpolar Current during positive SAM

527 induce an intensified eastward surface ocean current and, as a result of Ekman drift, a stronger

19

528   northward surface current south of 45°S. This promotes upwelling over the margin of the Modified

529   Circumpolar Deep Water, whose characteristics – warm and salty – can promote sea ice thawing in

530   the Ross Sea despite the general wind-driven surface cooling (Lefebvre and Goosse, 2005; Lefebvre et

531   al., 2004). Thus, the negative SAM during the late-Holocene might have reduced the upwelling with

532   direct effects on fast ice thawing. However, considering the small age uncertainties around the tephra

533   layer (687±7 yrs BP), the shift in our record almost certainly occurred before the change in the SAM

534   index. Therefore, the role of upwelling on fast ice dynamics remains somewhat elusive, although a

535   negative SAM after 0.7 ka presumably contributed to some preservation of coastal sea ice throughout

536   the summer. Overall, we believe that the abrupt atmospheric cooling recorded over the Victoria Land

537   Coast region (Stenni *et al.*, 2017) likely exerted first-order control on the rapid shift of fast ice

538   coverage in the inner Ross Sea during the late-Holocene, but other factors are more challenging to

539   identify at this stage, in part, owing to the complex behaviour of sea ice cover, more generally (Meehl

540   *et al.*, 2019).

541

542   5. Conclusions

543   This study provides the first high-resolution late-Holocene reconstruction of fast ice dynamics in the

544   Ross Sea (Edisto inlet) based on multiple proxies (IPSO$_{25}$, diatom census counts and bulk properties)

545   analysed in a 14.6 m long laminated diatom ooze record (HLF17-1). Our results indicate that the

546   emplacement of laminated strata in the Edisto inlet reflect different fast ice cover during the summer

547   months. In early summer, fast ice break-up releases sympagic diatoms living within the ice and

548   platelet ice beneath. As the inlet opens, algal blooms in melt ponds promote sinking of phytodetritus,

549   which accumulates with the sympagic diatoms. Overall, the opening of the inlet generates dark

550   laminae characterized by relatively high concentrations of the sympagic biomarker IPSO$_{25}$, high

551   lithogenic material and enriched δ^{13}C (OM) with a relatively heterogeneous distribution of diatoms. In

552   late summer, when ice-free conditions persist, the diatom *Corethron pennatum* can adapt to stratified

553   and oligotrophic waters, becoming the dominant species and generating thick mats at the seabed. The

554   resulting composition of light laminae is characterized by low IPSO$_{25}$ concentrations, low lithogenic

555   material, and depleted δ^{13}C (OM).

20

556   Building on the knowledge gained at lamina level, our down-core results show an abrupt change in

557   summer fast ice dynamics over the late-Holocene. In particular, while the inlet appears to have opened

558   regularly during summers since 2.6 ka BP, light laminae became suddenly less frequent around 0.7 ka

559   BP, indicating an abrupt shift towards less recurrent ice-free conditions in the inlet. Comparison with

560   ice core data from the region revealed that the abrupt shift in fast ice dynamics was likely the

561   expression of colder climate conditions. Our results, both at seasonal (laminae) and late-Holocene

562   scales, provide new insights into the application of the newly established $IPSO_{25}$ sea ice proxy, and in

563   particular its usefulness for paleo reconstructions of summer fast ice dynamics.

564

Acknowledgments

572

573

574

575

576

577

578

579

580

581

582

583

584

585

586

587

588

589

590 **Captions**

591 Fig.1. Study area in the Ross Sea. (a) Map showing the 40-y average of sea ice concentration (%) in

592 February based on satellite images. The red line displays the 10% contour. The location of HLF17-1

593 core and ice cores of the Victoria Land Coast is shown with filled red and green circles, respectively;

594 (b) Red filled circle shows the location of HLF17-1 in the Edisto inlet; (c) Chirp profile showing the

595 sediment strata geometry. Parallel reflectors show continuous sedimentation throughout the Holocene

596

597 Fig 2. HLF17-1 piston core (14.65 m) from top (section XV) to bottom (section I).

598

599 Fig. 3. Dark and light lamina analysis in section III. (a) Brightness (green line) and sub-sampled

600 horizons (n=34); relative frequency of (b) $IPSO_{25}$, (c) *Corethron pennatum* (d) $\delta^{13}C$ and (e) TiO_2 in

601 the light (red open bars) and dark (gray filled bars) laminae, respectively

602

603 Fig. 4. Composition of laminae sub-sampled in section III. Blue and red dashed lines display the two

604 dominant clusters which reflect contrasting sea ice coverages, namely fast ice thawing and ice-free

605 conditions, respectively.

606

607 Fig. 5. Satellite images (a, 2017; b, 2012; c, 2018) of Edisto inlet (red ellipse) which provide the

608 spectrum of sea ice coverage which, in turn, exerts first-order control on the formation of laminated

609 sediments. 2017 was characterized by an early opening followed by protracted ice free conditions of

610 the inlet. In 2012, thawing was incomplete and occurred toward the end of the summer. Finally, 2018

611 represented the end of the spectrum as sea ice persisted throughout the summer in the inlet

612

613   Fig. 6. Median calendar age (years before present) and 2σ error from the Bayesian age-depth model of

614   core HLF17-1. Gray colors show the dates used in the model. Additional carbonate dates (ophiurae

615   and planktonic foraminifera) were used to test, independently, the age-model and the assumption

616   behind the local marine reservoir age of the carbonate fraction.

617

618   Fig. 7. Fast ice dynamics in the Edisto inlet and general climate conditions over the late-Holocene.

619   Top filled blue circles show the dated horizons used in the age-depth model (a) $IPSO_{25}$ and brightness

620   (11-point weighted average to match the $IPSO_{25}$ resolution), red and blue filled circles were defined

621   according to the cluster analysis (see text for further details); (b) $\delta^{13}C$ and brightness (11-point

622   weighted average to match the $IPSO_{25}$ resolution), purple and pink filled squares were defined

623   according to the cluster analysis (see text for further details); (c) sediment accumulation rate and grain-

624   size; (d) 10-yr-binned averages of temperature anomalies in the ice cores (relative to 1900–1990 CE)

625   (brown symbols) from the Victoria Land Coast ice cores (see Fig.1a) and 5-point weight average

626   (yellow line) (Stenni et al., 2017); (e) Reconstruction of annual Southern Annular Mode index (7-yr-

627   binned average, blue line and 70-yr loess filter, red line) (Abdram et al 2014). Grey boxes define

628   period characterized by regular opening of the inlet over summer (e.g. Fig. 5a).

629

630

631

632   **References**

633   Abram, N.J., Mulvaney, R., Vimeux, F., Phipps, S.J., Turner, J., England, M.H., 2014. Evolution of the
634   Southern Annular Mode during the past millennium. Nature Climate Change 4, 564.
635   Alley, K., Patacca, K., Pike, J., Dunbar, R., Leventer, A., 2018. Iceberg Alley, East Antarctic Margin:
636   Continuously laminated diatomaceous sediments from the late Holocene. Marine Micropaleontology
637   140, 56-68.
638   Arias-Ortiz, A., Masqué, P., Garcia-Orellana, J., Serrano, O., Mazarrasa, I., Marbà, N., Lovelock, C.E.,
639   Lavery, P.S., Duarte, C.M., 2018. Reviews and syntheses: 210 Pb-derived sediment and carbon
640   accumulation rates in vegetated coastal ecosystems–setting the record straight.
641   Armand, L., 1997. The use of diatom transfer functions in estimating sea-surface temperature and
642   sea-ice in cores from the southeast Indian Ocean.

23

643 Armand, L.K., Crosta, X., Romero, O., Pichon, J.-J., 2005. The biogeography of major diatom taxa in
644 Southern Ocean sediments: 1. Sea ice related species. Palaeogeography, Palaeoclimatology,
645 Palaeoecology 223, 93-126.
646 Arrigo, K.R., DiTullio, G.R., Dunbar, R.B., Robinson, D.H., VanWoert, M., Worthen, D.L., Lizotte, M.P.,
647 2000. Phytoplankton taxonomic variability in nutrient utilization and primary production in the Ross
648 Sea. Journal of Geophysical Research: Oceans 105, 8827-8846.
649 Arrigo, K.R., van Dijken, G.L., 2004. Annual changes in sea-ice, chlorophyll a, and primary production
650 in the Ross Sea, Antarctica. Deep Sea Research Part II: Topical Studies in Oceanography 51, 117-138.
651 Atkins, C., Dunbar, G., 2009. Aeolian sediment flux from sea ice into Southern McMurdo Sound,
652 Antarctica. Global and Planetary Change 69, 133-141.
653 Bahk, J.J., Yoon, H.I., Kim, Y., Kang, C.Y., Bae, S.H., 2003. Microfabric analysis of laminated diatom
654 ooze (Holocene) from the eastern Bransfield Strait, Antarctic Peninsula. Geosciences Journal 7, 135-
655 142.
656 Belt, S., Smik, L., Brown, T., Kim, J.-H., Rowland, S., Allen, C., Gal, J.-K., Shin, K.-H., Lee, J., Taylor, K.,
657 2016. Source identification and distribution reveals the potential of the geochemical Antarctic sea ice
658 proxy IPSO 25. Nature communications 7, 12655.
659 Belt, S., 2018. Source-specific biomarkers as proxies for Arctic and Antarctic sea ice. Organic
660 geochemistry.
661 Belt, S.T., 2019. What do IP25 and related biomarkers really reveal about sea ice change? Quaternary
662 Science Reviews 204, 216-219.
663 Belt, S.T., Brown, T.A., Rodriguez, A.N., Sanz, P.C., Tonkin, A., Ingle, R., 2012. A reproducible method
664 for the extraction, identification and quantification of the Arctic sea ice proxy IP 25 from marine
665 sediments. Analytical Methods 4, 705-713.
666 Belt, S.T., Brown, T.A., Smik, L., Tatarek, A., Wiktor, J., Stowasser, G., Assmy, P., Allen, C.S., Husum, K.,
667 2017. Identification of C25 highly branched isoprenoid (HBI) alkenes in diatoms of the genus
668 Rhizosolenia in polar and sub-polar marine phytoplankton. Organic geochemistry 110, 65-72.
669 Belt, S.T., Cabedo-Sanz, P., Smik, L., Navarro-Rodriguez, A., Berben, S.M., Knies, J., Husum, K., 2015.
670 Identification of paleo Arctic winter sea ice limits and the marginal ice zone: optimised biomarker-
671 based reconstructions of late Quaternary Arctic sea ice. Earth and Planetary Science Letters 431, 127-
672 139.
673 Belt, S.T., Müller, J., 2013. The Arctic sea ice biomarker IP25: a review of current understanding,
674 recommendations for future research and applications in palaeo sea ice reconstructions. Quaternary
675 Science Reviews 79, 9-25.
676 Belt, S.T., Smik, L., Köseoğlu, D., Knies, J., Husum, K., 2019. A novel biomarker-based proxy for the
677 spring phytoplankton bloom in Arctic and sub-arctic settings – HBI T25. Earth and Planetary Science
678 Letters 523, 115703.
679 Bertler, N.A., Conway, H., Dahl-Jensen, D., Emanuelsson, D.B., Winstrup, M., Vallelonga, P.T., Lee,
680 J.E., Brook, E.J., Severinghaus, J.P., Fudge, T.J., 2018. The Ross Sea Dipole-temperature, snow
681 accumulation and sea ice variability in the Ross Sea region, Antarctica, over the past 2700 years.
682 Climate of the Past 14, 193-214.
683 Bintanja, R., Van Oldenborgh, G., Drijfhout, S., Wouters, B., Katsman, C., 2013. Important role for
684 ocean warming and increased ice-shelf melt in Antarctic sea-ice expansion. Nature Geoscience 6,
685 376.
686 Collins, L.G., Allen, C.S., Pike, J., Hodgson, D.A., Weckström, K., Massé, G., 2013. Evaluating highly
687 branched isoprenoid (HBI) biomarkers as a novel Antarctic sea-ice proxy in deep ocean glacial age
688 sediments. Quaternary Science Reviews 79, 87-98.
689 Crosta, X., Crespin, J., Billy, I., Ther, O., 2005. Major factors controlling Holocene δ13Corg changes in
690 a seasonal sea-ice environment, Adélie Land, East Antarctica. Global Biogeochemical Cycles 19.
691 Crosta, X., Koç, N., 2007. Chapter Eight Diatoms: From Micropaleontology to Isotope Geochemistry,
692 In: Hillaire–Marcel, C., De Vernal, A. (Eds.), Developments in Marine Geology. Elsevier, pp. 327-369.

D'Angelo, A., Giglio, F., Miserocchi, S., Sanchez-Vidal, A., Aliani, S., Tesi, T., Viola, A., Mazzola, M., Langone, L., 2018. Multi-year particle fluxes in Kongsfjorden, Svalbard. Biogeosciences 15, 5343-5363.

Denis, D., Crosta, X., Barbara, L., Massé, G., Renssen, H., Ther, O., Giraudeau, J., 2010. Sea ice and wind variability during the Holocene in East Antarctica: insight on middle–high latitude coupling. Quaternary Science Reviews 29, 3709-3719.

Denis, D., Crosta, X., Zaragosi, S., Romero, O., Martin, B., Mas, V., 2006. Seasonal and subseasonal climate changes recorded in laminated diatom ooze sediments, Adelie Land, East Antarctica. The Holocene 16, 1137-1147.

Di Roberto, A., Colizza, E., Del Carlo, P., Petrelli, M., Finocchiaro, F., Kuhn, G., 2019. First marine cryptotephra in Antarctica found in sediments of the western Ross Sea correlates with englacial tephras and climate records. Scientific Reports 9, 10628.

Dinelli, E., Lucchini, F., Fabbri, M., Cortecci, G., 2001. Metal distribution and environmental problems related to sulfide oxidation in the Libiola copper mine area (Ligurian Apennines, Italy). Journal of Geochemical Exploration 74, 141-152.

Domack, E., Leventer, A., Dunbar, R., Taylor, F., Brachfeld, S., Sjunneskog, C., 2001. Chronology of the Palmer Deep site, Antarctic Peninsula: a Holocene palaeoenvironmental reference for the circum-Antarctic. The Holocene 11, 1-9.

Etourneau, J., Collins, L.G., Willmott, V., Kim, J.H., Barbara, L., Leventer, A., Schouten, S., Sinninghe Damsté, J.S., Bianchini, A., Klein, V., Crosta, X., Massé, G., 2013. Holocene climate variations in the western Antarctic Peninsula: evidence for sea ice extent predominantly controlled by changes in insolation and ENSO variability. Clim. Past 9, 1431-1446.

Finocchiaro, F., Langone, L., Colizza, E., Fontolan, G., Giglio, F., Tuzzi, E., 2005. Record of the early Holocene warming in a laminated sediment core from Cape Hallett Bay (Northern Victoria Land, Antarctica). Global and Planetary Change 45, 193-206.

Frignani, M., Langone, L., Ravaioli, M., Sorgente, D., Alvisi, F., Albertazzi, S., 2005. Fine-sediment mass balance in the western Adriatic continental shelf over a century time scale. Marine Geology 222, 113-133.

Geilfus, N.-X., Tison, J.-L., Ackley, S., Galley, R., Rysgaard, S., Miller, L., Delille, B., 2014. Sea ice pCO$_2$ dynamics and air–ice CO$_2$ fluxes during the Sea Ice Mass Balance in the Antarctic (SIMBA) experiment–Bellingshausen Sea, Antarctica. The Cryosphere 8, 2395-2407.

Geilfus, N.X., Galley, R.J., Crabeck, O., Papakyriakou, T., Landy, J., Tison, J.L., Rysgaard, S., 2015. Inorganic carbon dynamics of melt-pond-covered first-year sea ice in the Canadian Arctic. Biogeosciences 12, 2047-2061.

Gersonde, R., Zielinski, U., 2000. The reconstruction of late Quaternary Antarctic sea-ice distribution—the use of diatoms as a proxy for sea-ice. Palaeogeography, Palaeoclimatology, Palaeoecology 162, 263-286.

Hall, B.L., Henderson, G.M., Baroni, C., Kellogg, T.B., 2010. Constant Holocene Southern-Ocean 14C reservoir ages and ice-shelf flow rates. Earth and Planetary Science Letters 296, 115-123.

Haslett, J., Parnell, A., 2008. A simple monotone process with application to radiocarbon-dated depth chronologies. Journal of the Royal Statistical Society: Series C (Applied Statistics) 57, 399-418.

Hawley, R.L., Waddington, E.D., Alley, R.B., Taylor, K.C., 2003. Annual layers in polar firn detected by borehole optical stratigraphy. Geophysical Research Letters 30.

Hjort, C., Ingólfsson, Ó., Möller, P., Lirio, J.M., 1997. Holocene glacial history and sea-level changes on James Ross Island, Antarctic Peninsula. Journal of Quaternary Science: Published for the Quaternary Research Association 12, 259-273.

Lamping, N., Müller, J., Esper, O., Hillenbrand, C.-D., Smith, J.A., Kuhn, G., 2020. Highly branched isoprenoids reveal onset of deglaciation followed by dynamic sea-ice conditions in the western Amundsen Sea, Antarctica. Quaternary Science Reviews 228, 106103.

Lefebvre, W., Goosse, H., 2005. Influence of the Southern Annular Mode on the sea ice-ocean system: the role of the thermal and mechanical forcing. Ocean Sci. 1, 145-157.

Lefebvre, W., Goosse, H., Timmermann, R., Fichefet, T., 2004. Influence of the Southern Annular Mode on the sea ice–ocean system. Journal of Geophysical Research: Oceans 109.

Lehmann, M.F., Bernasconi, S.M., McKenzie, J.A., Barbieri, A., Simona, M., Veronesi, M., 2004. Seasonal variation of the δC and δN of particulate and dissolved carbon and nitrogen in Lake Lugano: Constraints on biogeochemical cycling in a eutrophic lake. Limnology and Oceanography 49, 415-429.

Leventer, A., 1998. The fate of Antarctic "sea ice diatoms" and their use as paleoenvironmental indicators. Antarctic sea ice. Biological processes, interactions and variability, 121-137.

Leventer, A., Domack, E., Barkoukis, A., McAndrews, B., Murray, J., 2002. Laminations from the Palmer Deep: A diatom-based interpretation. Paleoceanography 17, PAL 3-1-PAL 3-15.

Leventer, A., Domack, E., Pike, J., Stickley, C., Maddison, E., Brachfeld, S.A., Manley, P., McClennen, C., 2006. Marine sediment record from the East Antarctic margin reveals dynamics of ice sheet recession.

Licht, K.J., Cunningham, W.L., Andrews, J.T., Domack, E.W., Jennings, A.E., 1998. Establishing chronologies from acid-insoluble organic 14C dates on Antarctic (Ross Sea) and Arctic (North Atlantic) marine sediments. Polar Research 17, 203-216.

Maddison, E.J., Pike, J., Dunbar, R., 2012. Seasonally laminated diatom-rich sediments from Dumont d'Urville Trough, East Antarctic margin: Late-Holocene neoglacial sea-ice conditions. The Holocene 22, 857-875.

Maddison, E.J., Pike, J., Leventer, A., Domack, E.W., 2005. Deglacial seasonal and sub-seasonal diatom record from Palmer Deep, Antarctica. Journal of Quaternary Science: Published for the Quaternary Research Association 20, 435-446.

Maddison, E.J., Pike, J., Leventer, A., Dunbar, R., Brachfeld, S., Domack, E.W., Manley, P., McClennen, C., 2006. Post-glacial seasonal diatom record of the Mertz Glacier Polynya, East Antarctica. Marine Micropaleontology 60, 66-88.

Massé, G., Belt, S.T., Crosta, X., Schmidt, S., Snape, I., Thomas, D.N., Rowland, S.J., 2011. Highly branched isoprenoids as proxies for variable sea ice conditions in the Southern Ocean. Antarctic Science 23, 487-498.

McGregor, H.V., Evans, M.N., Goosse, H., Leduc, G., Martrat, B., Addison, J.A., Mortyn, P.G., Oppo, D.W., Seidenkrantz, M.-S., Sicre, M.-A., 2015. Robust global ocean cooling trend for the pre-industrial Common Era. Nature Geoscience 8, 671-677.

McKay, R., Golledge, N.R., Maas, S., Naish, T., Levy, R., Dunbar, G., Kuhn, G., 2016. Antarctic marine ice-sheet retreat in the Ross Sea during the early Holocene. Geology 44, 7-10.

Meehl, G.A., Arblaster, J.M., Bitz, C.M., Chung, C.T., Teng, H., 2016. Antarctic sea-ice expansion between 2000 and 2014 driven by tropical Pacific decadal climate variability. Nature Geoscience 9, 590.

Meehl, G.A., Arblaster, J.M., Chung, C.T.Y., Holland, M.M., DuVivier, A., Thompson, L., Yang, D., Bitz, C.M., 2019. Sustained ocean changes contributed to sudden Antarctic sea ice retreat in late 2016. Nature Communications 10, 14.

Mezgec, K., Stenni, B., Crosta, X., Masson-Delmotte, V., Baroni, C., Braida, M., Ciardini, V., Colizza, E., Melis, R., Salvatore, M.C., Severi, M., Scarchilli, C., Traversi, R., Udisti, R., Frezzotti, M., 2017. Holocene sea ice variability driven by wind and polynya efficiency in the Ross Sea. Nature Communications 8, 1334.

Mortlock, R.A., Froelich, P.N., 1989. A simple method for the rapid determination of biogenic opal in pelagic marine sediments. Deep Sea Research Part A. Oceanographic Research Papers 36, 1415-1426.

Narcisi, B., Petit, J.R., Delmonte, B., Scarchilli, C., Stenni, B., 2012. A 16,000-yr tephra framework for the Antarctic ice sheet: a contribution from the new Talos Dome core. Quaternary Science Reviews 49, 52-63.

Parkinson, C.L., 2019. A 40-y record reveals gradual Antarctic sea ice increases followed by decreases at rates far exceeding the rates seen in the Arctic. Proceedings of the National Academy of Sciences 116, 14414-14423.

794   Popp, B.N., Hanson, K.L., Dore, J.E., Bidigare, R.R., Laws, E.A., Wakeham, S.G., 1999. Controls on the
795   Carbon Isotopic Composition of Phytoplankton, In: Abrantes, F., Mix, A.C. (Eds.), Reconstructing
796   Ocean History: A Window into the Future. Springer US, Boston, MA, pp. 381-398.

797   Popp, B.N., Laws, E.A., Bidigare, R.R., Dore, J.E., Hanson, K.L., Wakeham, S.G., 1998. Effect of
798   Phytoplankton Cell Geometry on Carbon Isotopic Fractionation. Geochimica et Cosmochimica Acta
799   62, 69-77.

800   Reimer, P.J., Bard, E., Bayliss, A., Beck, J.W., Blackwell, P.G., Ramsey, C.B., Buck, C.E., Cheng, H.,
801   Edwards, R.L., Friedrich, M., 2013. IntCal13 and Marine13 radiocarbon age calibration curves 0–
802   50,000 years cal BP. Radiocarbon 55, 1869-1887.

803   Riaux-Gobin, C., Dieckmann, G.S., Poulin, M., Neveux, J., Labrune, C., Vétion, G., 2013. Environmental
804   conditions, particle flux and sympagic microalgal succession in spring before the sea-ice break-up in
805   Adélie Land, East Antarctica. Polar Research 32, 19675.

806   Riaux-Gobin, C., Poulin, M., Dieckmann, G., Labrune, C., Vétion, G., 2011. Spring phytoplankton onset
807   after the ice break-up and sea-ice signature (Adélie Land, East Antarctica). Polar Research 30, 5910.

808   Salter, I., Kemp, A.E., Moore, C.M., Lampitt, R.S., Wolff, G.A., Holtvoeth, J., 2012. Diatom resting
809   spore ecology drives enhanced carbon export from a naturally iron-fertilized bloom in the Southern
810   Ocean. Global Biogeochemical Cycles 26.

811   Schrader, H., Gersonde, R., 1978. Diatoms and silicoflagellates. In Zachariasse etb al.
812   Microplaeontological counting methods and techniques-an excercise on an eight metres section of
813   the lower Pliocene of Capo Rossello. Sicily. Utrecht Micropal. Bull. 17:, 129-176.

814   Smik, L., Belt, S.T., Lieser, J.L., Armand, L.K., Leventer, A., 2016. Distributions of highly branched
815   isoprenoid alkenes and other algal lipids in surface waters from East Antarctica: Further insights for
816   biomarker-based paleo sea-ice reconstruction. Organic geochemistry 95, 71-80.

817   Smith, W., Anderson, R.F., Moore, J.K., Codispoti, L.A., Morrison, J.M., 2000. The US southern ocean
818   joint global ocean flux study: an introduction to AESOPS. Deep Sea Research Part II: Topical Studies in
819   Oceanography 47, 3073-3093.

820   Stammerjohn, S.E., Martinson, D., Smith, R., Yuan, X., Rind, D., 2008. Trends in Antarctic annual sea
821   ice retreat and advance and their relation to El Niño–Southern Oscillation and Southern Annular
822   Mode variability. Journal of Geophysical Research: Oceans 113.

823   Stenni, B., Curran, M.A.J., Abram, N.J., Orsi, A., Goursaud, S., Masson-Delmotte, V., Neukom, R.,
824   Goosse, H., Divine, D., van Ommen, T., Steig, E.J., Dixon, D.A., Thomas, E.R., Bertler, N.A.N., Isaksson,
825   E., Ekaykin, A., Werner, M., Frezzotti, M., 2017. Antarctic climate variability on regional and
826   continental scales over the last 2000 years. Clim. Past 13, 1609-1634.

827   Stuiver, M., Polach, H.A., 1977. Discussion reporting of 14 C data. Radiocarbon 19, 355-363.

828   Tanimura, Y., FUKUCHI, M., WATANABE, K., Moriwaki, K., 1990. Diatoms in water column and sea-ice
829   in Lützow-Holm Bay, Antarctica, and their preservation in the underlying sediments. Bulletin of the
830   National Science Museum. Series C 16, 15-39.

831   Tesi, T., Langone, L., Ravaioli, M., Giglio, F., Capotondi, L., 2012. Particulate export and lateral
832   advection in the Antarctic Polar Front (Southern Pacific Ocean): One-year mooring deployment.
833   Journal of Marine Systems 105, 70-81.

834   Thomas, D.N., Kennedy, H., Kattner, G., Gerdes, D., Gough, C., Dieckmann, G.S., 2001.
835   Biogeochemistry of platelet ice: its influence on particle flux under fast ice in the Weddell Sea,
836   Antarctica. Polar Biology 24, 486-496.

837   Turner, J., Comiso, J.C., Marshall, G.J., Lachlan-Cope, T.A., Bracegirdle, T., Maksym, T., Meredith,
838   M.P., Wang, Z., Orr, A., 2009. Non-annular atmospheric circulation change induced by stratospheric
839   ozone depletion and its role in the recent increase of Antarctic sea ice extent. Geophysical Research
840   Letters 36.

841   Turner, J., Phillips, T., Marshall, G.J., Hosking, J.S., Pope, J.O., Bracegirdle, T.J., Deb, P., 2017.
842   Unprecedented springtime retreat of Antarctic sea ice in 2016. Geophysical Research Letters 44,
843   6868-6875.

844   Vorrath, M.E., Müller, J., Esper, O., Mollenhauer, G., Haas, C., Schefuß, E., Fahl, K., 2019. Highly
845   branched isoprenoids for Southern Ocean sea ice reconstructions: a pilot study from the Western
846   Antarctic Peninsula. Biogeosciences 16, 2961-2981.

847

848

849

850   Fig 1.
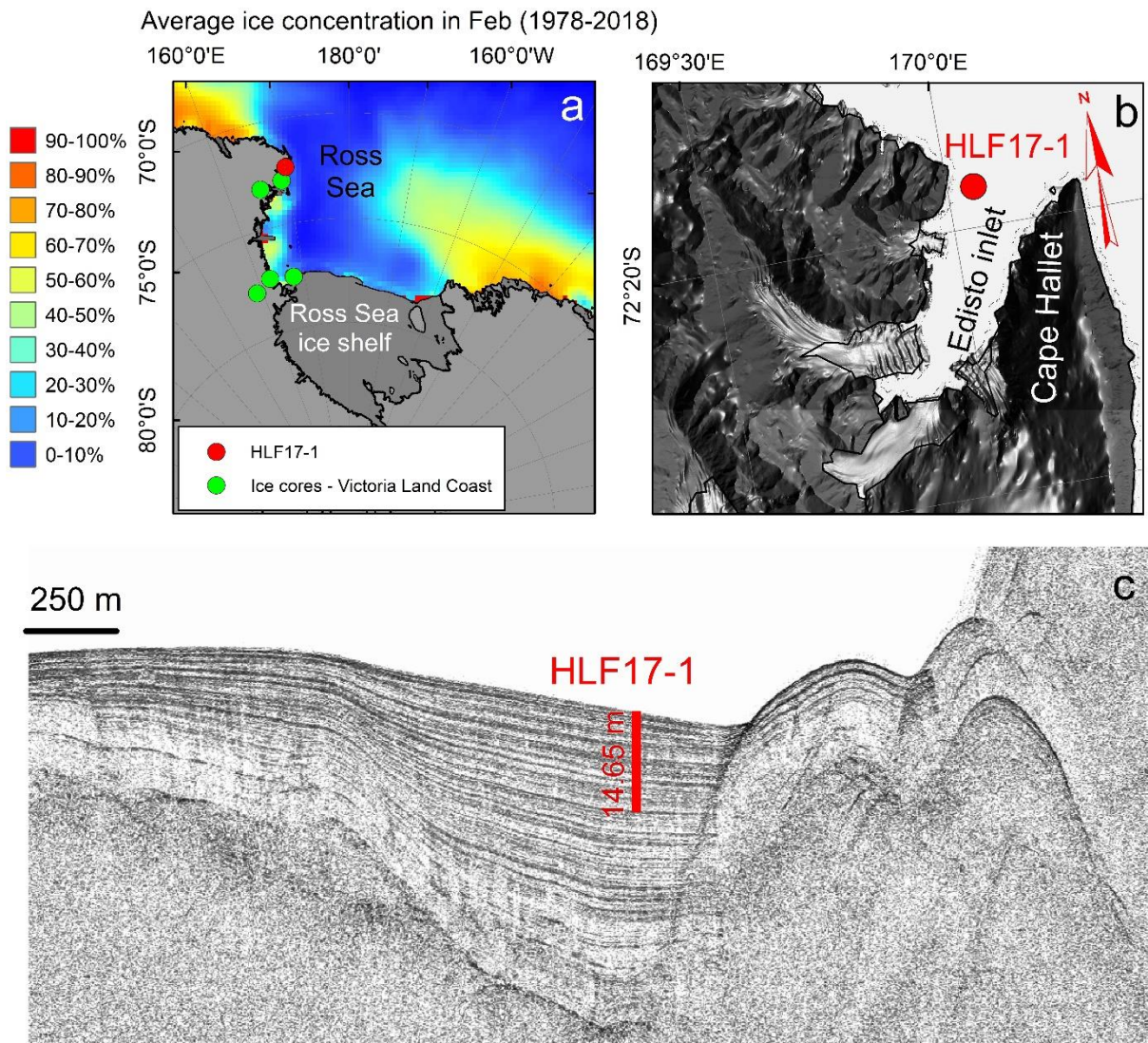
851

852

853   Fig. 2
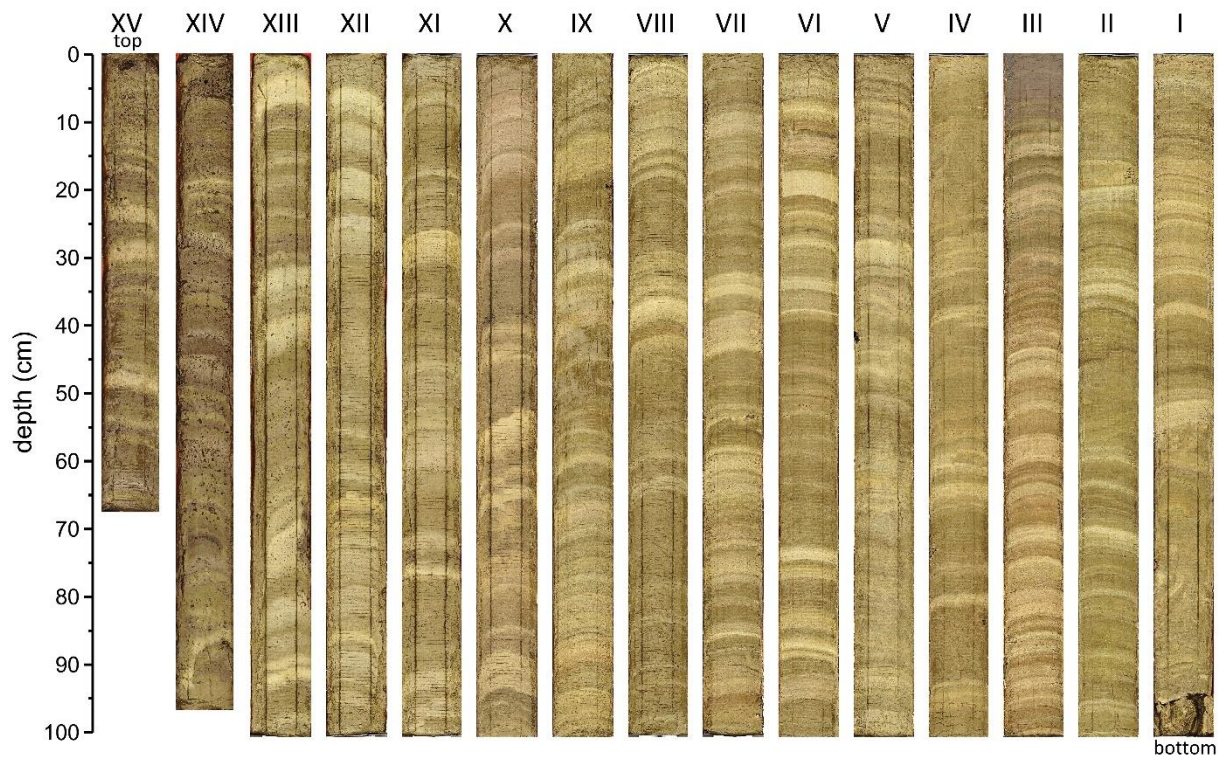
854

855

856   Fig. 3
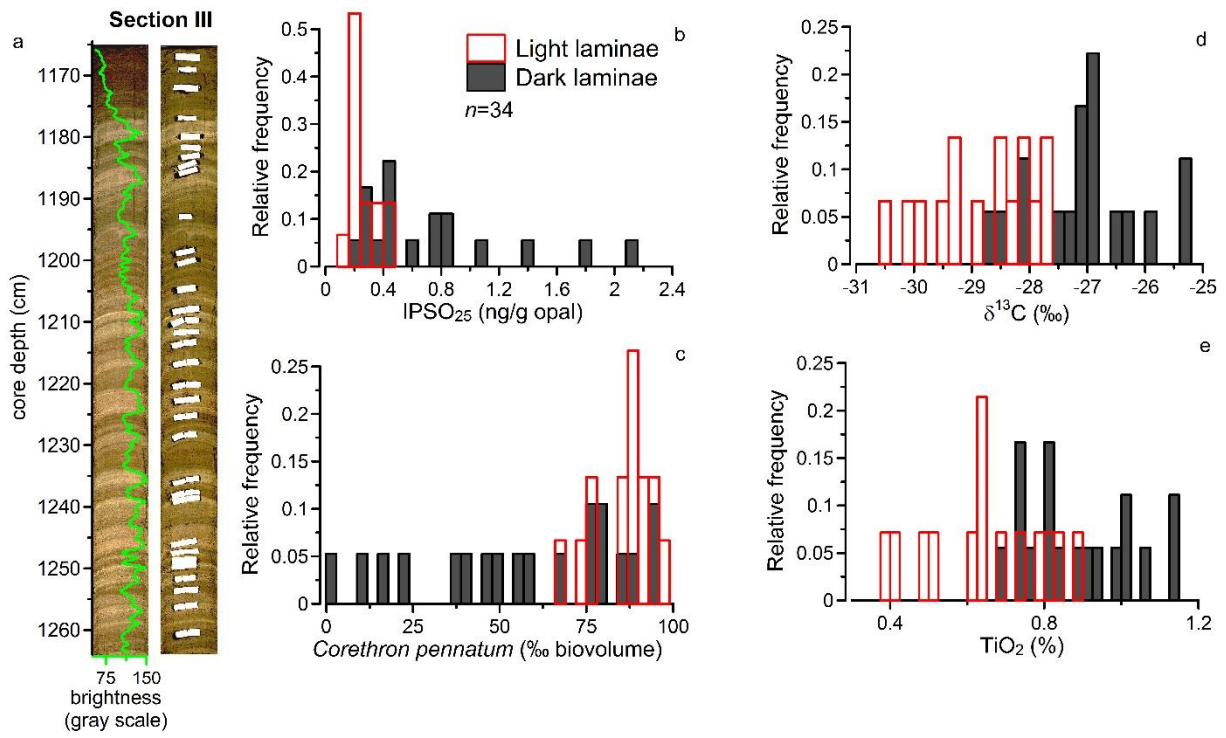
857

858

859   Fig. 4

860

861

862   Fig. 5

opened throughout the summer — partially opened in late summer — closed throughout the summer

a 2017 — b 2012 — c 2018
Jan-21 — Jan-29 — Feb-07
2017 — 2012 — 2018
Feb-02 — Feb-28 — March-10

dark & light laminae — only dark laminae — lack of accumulation

863

864

865   Fig. 6

866

867

" Disclaimer: This is a pre-publication version. Readers are recommended to consult the full published version for accuracy and citation."
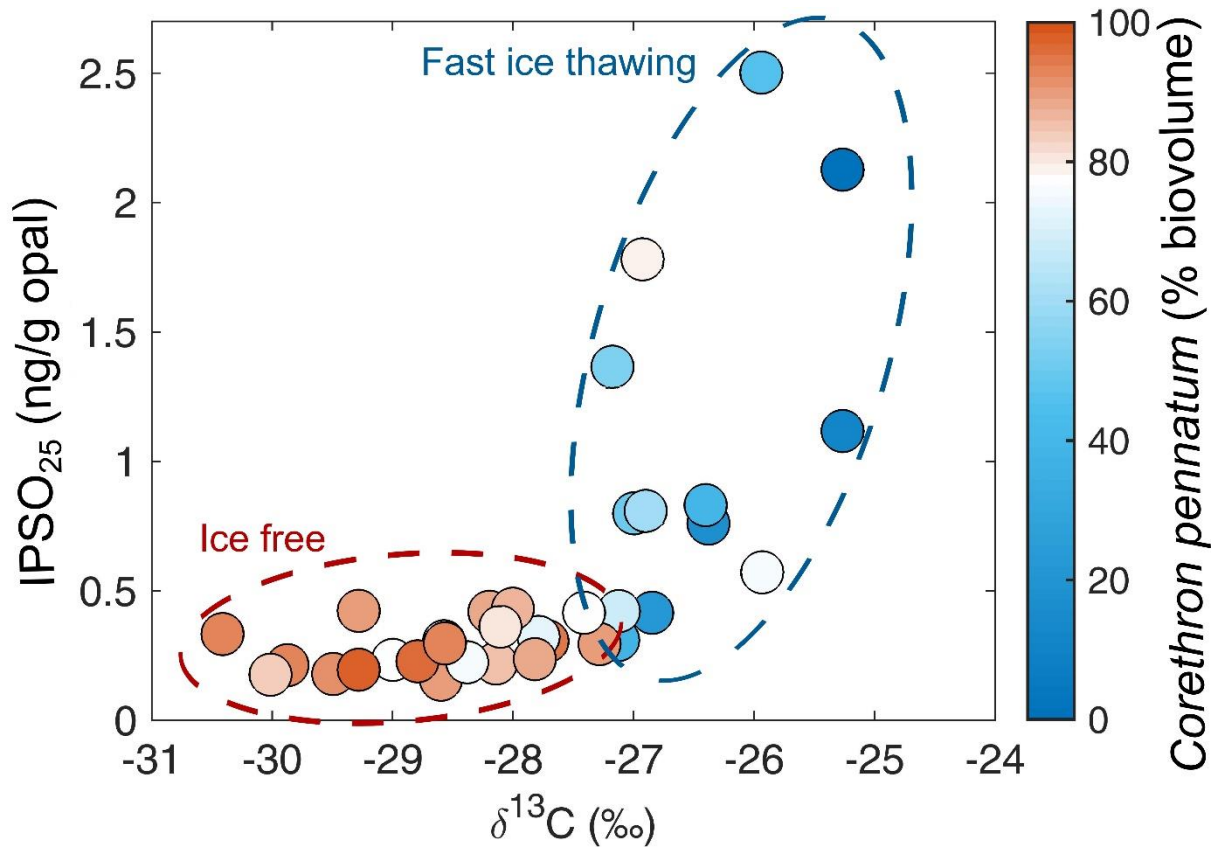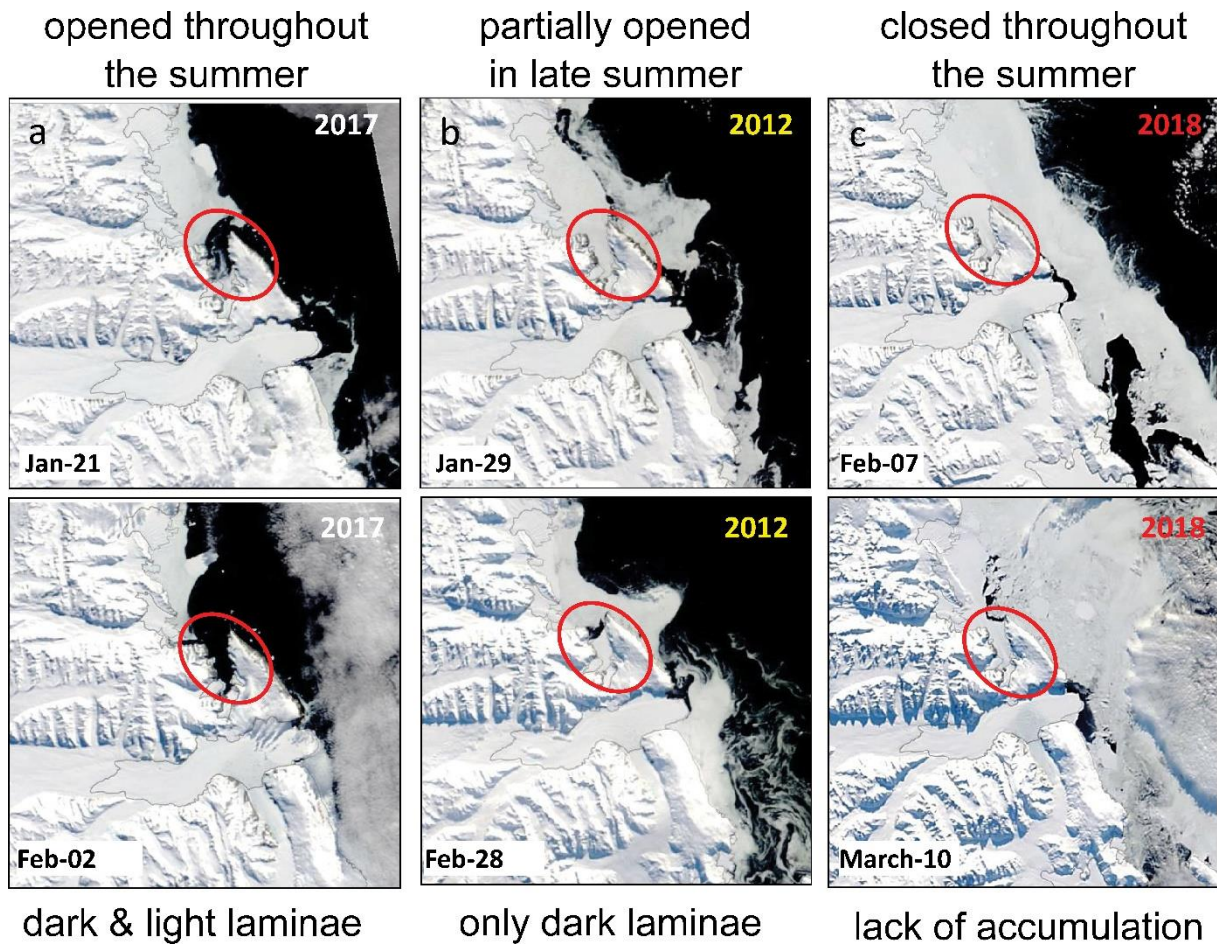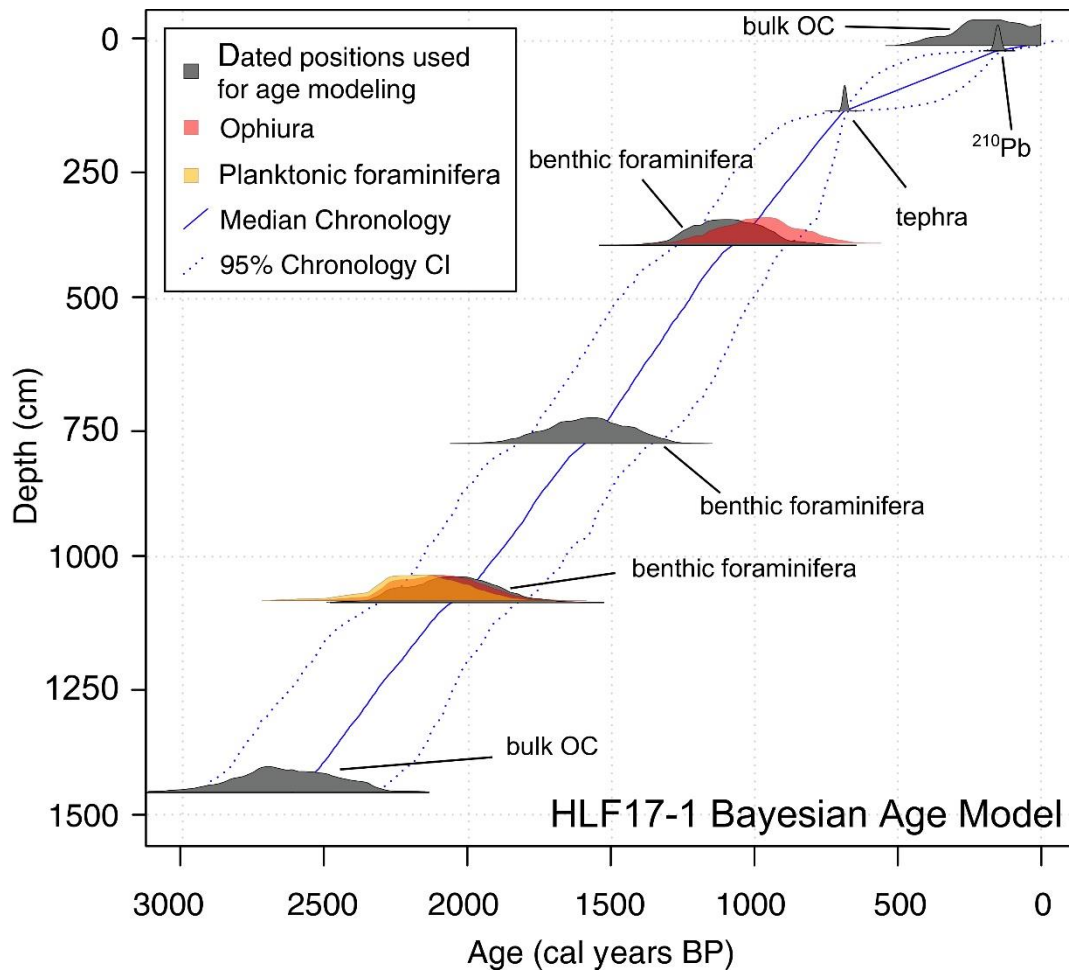
868   Fig. 7
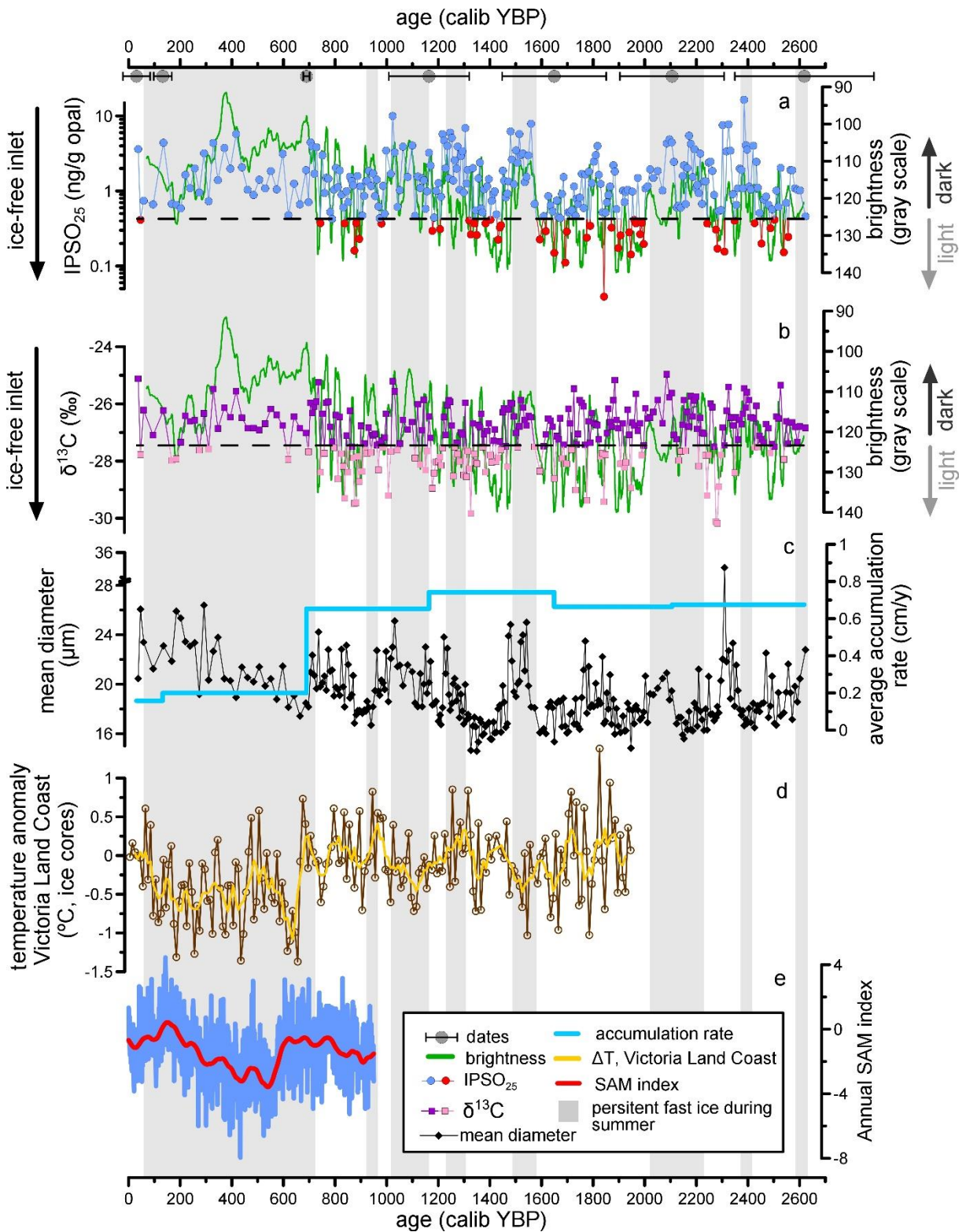
869

870

871   **Highlights**

872   Dark and light sediment laminae exhibit different chemical and ecological features

873   Dark and light sediment laminae reflect different fast ice coverage during summer

874   Enriched δ^{13}C and high IPSO$_{25}$ (dark laminae) track early thawing of fast ice

875   High concentration of *C. pennatum* (light laminae) identifies protracted ice-free conditions

876   Summer ice-free conditions became less frequent since 0.7 ka BP along the north-western Ross Sea

877

878

Table 1. Dated horizons using AMS, ^{210}Pb and tephra layer

core	horizon	depth (cm)*	depth range (cm)	type of sample	ID lab	dating method	age (y)	error (y)	modelled median age	minimum 95% CI	maximum 95% CI
HLF16-1	VII 0-10	402	±5	benthic forams**	Poz-110839	^{14}C	2330 yBP	30	1083	927	1253.65
HLF16-1	VII 0-10	402	±5	ophiuroideae	Poz-110430	^{14}C	2220 yBP	30			
HLF16-1	VII 0-10	402	±5	bulk OC	Poz-110836	^{14}C	2890 yBP	30			
HLF16-1	IV 60-70	775	±5	benthic forams**	OS-147514	^{14}C	2800 yBP	15	1589	1387.35	1778.65
HLF16-1	IV 60-70	775	±5	bulk OC	Poz-111163	^{14}C	3210 yBP	35			
HLF16-1	I 70-80	1091	±5	benthic forams**	Poz-110838	^{14}C	3200 yBP	30	2055.5	1853.45	2260
HLF16-1	I 75-75.5	1091.25	±0.25	ophiuroideae	Poz-110431	^{14}C	3250 yBP	30			
HLF16-1	I 70-80	1091	±5	planktic forams	OS-147503	^{14}C	3300 yBP	35			
HLF16-1	I 70-80	1091	±5	bulk OC	Poz-110837	^{14}C	3875 yBP	30			
HLF17-2BC	0-1	0.5	±0.25	bulk OC	Poz-108920	^{14}C	200 yBP	30			
HLF17-1	XV 8-10	9	±0.5	bulk OC**	OS-141035	^{14}C	1940 yBP	15	58	5	134
HLF17-1	XV 18-20	19	±1	sediment**		^{210}Pb	150 y before 2017	20	154	119	190
HLF17-1	XIV 72-73	136.5	±1	sediment**		tephra***	687	7	687	675	698
HLF17-1	I 90-91	1456	±0.5	bulk OC**	Poz-92969	^{14}C	4220 yBP	50	2623.5	2353.8	2868.1

* depth refers to HLF17-1

** used in the age depth model

*** Di Roberto et al., 2019

879

880

881

Table 2. Composition of laminae from section III of HLF17-1. Data were grouped according to the lamina colour: light vs dark. Statistically significant differences between groups for each variable were assessed based on T-test (p<0.01).

laminae	depth	N_{tot}	OC	$\delta^{13}C$	Opal	porosity	$IPSO_{25}$	sand	silt	clay	Chaetoceros RS	Corethron pennatum	Fragilariopsis curta	Fragilariopsis cylindrus	Fragilariopsis obliquecostata	Fragilariopsis separanda	SiO_2	TiO_2	Al_2O_3	Fe_2O_3	K_2O
	cm	%	%	‰	%		ng/g opal	%	%	%	%	%	%	%	%	%	%	%	%	%	%
light																					
HLF17 1 III 14-15	1179.5	0.12	0.44	-28.6	43.8	0.91	0.16	11.2	75.7	13.2	3.6	17.3	56.7	2.9	9.2	0.8	59.0	0.4	2.7	1.8	1.1
HLF17 1 III 17-18	1182.5	0.12	0.52	-27.7	45.2	0.92	0.31	13.2	77.1	9.7	9.0	6.1	9.0	2.5	7.7	1.9	65.3	0.6	3.7	3.1	1.0
HLF 17 1 III 20-21	1185.5	0.10	0.48	-29.0	43.7	0.93	0.23	13.3	77.3	9.4	8.2	5.8	1.2	3.2	4.3	3.2	62.7	0.8	4.9	4.2	1.1
HLF17 1 III 33-34	1198.5	0.13	0.58	-28.1	40.1	0.90	0.22	11.3	78.6	10.1	5.3	1.3	5.2	0.7	2.9	0.0	64.4	0.7	4.3	3.6	1.1
HLF17 1 III 34.5-35	1200	0.16	0.66	-27.8	46.2	0.91	0.32	17.2	74.6	8.2	7.0	8.2	3.4	5.1	4.3	1.8	67.0	0.8	4.6	4.6	1.1
HLF 17 1 III 46-47	1211.5	0.12	0.48	-30.4	47.2	0.94	0.33	18.3	72.5	9.2	4.5	6.7	2.3	7.3	2.3	2.5	64.4	0.5	3.0	2.4	0.9
HLF 17 1 III 51-52	1216.5	0.10	0.58	-29.3	50.4	0.93	0.42	15.3	75.2	9.6	7.4	0.8	6.8	4.0	6.7	0.9	n.m.	n.m.	n.m.	n.m.	n.m.
HLF17 1 III 57-58	1222.5	0.11	0.45	-29.5	37.9	0.93	0.18	11.7	78.9	9.4	9.5	0.3	6.1	6.3	1.0	3.8	63.2	0.7	3.5	3.6	0.8
HLF 17 1 III 63-64	1228.5	0.14	0.63	-28.6	47.6	0.92	0.31	12.5	78.5	9.1	8.3	5.5	0.1	6.0	2.1	8.6	68.4	0.7	3.6	3.4	1.0
HLF17 1 III 71-72	1236.5	0.12	0.49	-29.9	45.1	0.94	0.21	13.4	77.9	8.7	9.4	6.8	5.3	2.8	9.3	2.2	66.4	0.4	2.3	1.9	0.7
HLF17 1 III 73.5-74.5	1239	0.13	0.60	-30.0	49.6	0.93	0.18	15.5	75.4	9.0	7.4	9.0	5.0	3.3	8.2	3.3	67.6	0.5	2.8	2.3	0.8
HLF17 1 III 80.5-81.5	1246	0.10	0.40	-29.3	30.2	0.92	0.20	13.2	75.0	1.7	1.3	4.6	4.2	2.1	0.5	7.8	60.6	0.8	4.5	3.9	1.1
HLF17 1 III 84-5-85.5	1250	0.11	0.56	-27.8	44.6	0.93	0.24	12.9	77.3	9.9	2.5	4.0	1.6	6.4	1.4	7.8	68.4	0.6	3.6	3.1	1.0
HLF 17 1 III 86.5-87.5	1252	0.10	0.51	-28.4	37.1	0.92	0.22	12.9	76.2	0.8	4.7	8.3	4.9	3.4	8.6	7.7	68.4	0.6	3.8	3.0	0.9
HLF17 1 III 91-92	1256.5	0.11	0.48	-28.2	34.1	0.91	0.42	12.9	74.7	2.3	0.5	8.6	5.8	1.9	9.6	1.2	63.2	0.9	5.0	4.2	1.2
mean		**0.12**	**0.52**	**-28.8**	**42.9**	**0.92**	**0.26**	**13.6**	**76.3**	**10.0**	**9.2**	**6.9**	**6.5**	**5.9**	**1.2**	**3.8**	**64.9**	**0.6**	**3.7**	**3.2**	**1.0**
s.d.		**0.02**	**0.08**	**0.9**	**5.8**	**0.01**	**0.08**	**2.1**	**1.8**	**1.4**	**5.0**	**1.4**	**2.4**	**3.7**	**3.0**	**3.3**	**3.0**	**0.2**	**0.8**	**0.9**	**0.1**
dark																					
HLF17 1 III 1-2	1166.5	0.14	0.73	-26.4	36.2	0.87	0.76	13.4	79.0	7.6	3.0	0.8	8.4	3.4	9.9	3.4	65.6	1.1	6.0	5.3	1.3
HLF17 1 III 3-4	1168.5	0.13	0.74	-26.8	34.7	0.89	0.42	14.6	77.5	8.0	8.0	1.0	1.6	3.9	8.4	4.6	64.8	0.9	5.2	4.7	1.3
HLF17 1 III 6-7	1171.5	0.13	0.69	-25.3	28.0	0.85	2.13	15.0	77.6	7.4	2.4	0.2	2.4	2.5	9.1	4.5	65.5	1.2	6.8	5.7	1.5
HLF17 1 III 11-12	1176.5	0.12	0.66	-25.9	30.4	0.89	0.57	11.2	79.4	9.4	4.9	6.4	6.0	4.5	3.1	1.5	65.6	0.8	4.5	3.9	1.2
HLF 17 1 III 16-17	1181.5	0.14	0.84	-27.0	35.3	0.90	0.80	13.8	77.8	8.4	3.9	3.6	1.3	2.4	2.4	1.4	67.3	0.8	4.7	4.5	1.2
HLF17 1 III 18-19	1183.5	0.13	0.69	-27.4	37.4	0.89	0.31	17.2	75.3	7.5	5.2	1.3	9.5	7.0	9.0	5.4	66.1	0.8	4.8	4.3	1.2
HLF17 1 III 27-28	1192.5	0.14	0.78	-26.9	30.1	0.88	0.81	13.6	78.0	8.5	9.7	3.4	2.1	4.7	7.6	0.0	66.1	1.0	5.7	4.8	1.4
HLF17 1 III 39-40	1204.5	0.11	0.74	-28.0	27.0	0.91	0.43	12.2	76.6	1.7	4.7	9.3	1.8	0.7	3.7	1.9	64.2	1.0	5.7	4.9	1.3

Sample																					
HLF17 1 III 42.5‑43.5	1208	12	60	27.1	34.2	0.91	0.42	17.3	4.2	8.5	1.1	4.9	1.6	4.7	8.5	1.3	68.2	0.7	3.9	3.4	1.0
HLF17 1 III 43.5‑44	1208.75	13	64	27.3	36.3	0.92	0.29	14.1	6.3	9.6	4.3	9.2	7.2	1.0	7.8	1.3	65.3	0.8	4.1	3.7	1.1
HLF17 1 III 44.5‑45	1209.75	10	51	28.8	41.8	0.93	0.23	14.9	5.6	9.5	2.6	6.3	5.2	5.9	4.1	1.1	60.6	1.0	6.2	5.0	1.4
HLF17 1 III 48‑49	1213.5	10	46	28.1	30.2	0.92	0.36	13.1	7.8	9.1	4.2	5.7	6.5	9.9	9.3	1.5	64.5	0.7	4.1	4.0	0.9
HLF17 1 III 55‑56	1220.5	13	68	25.3	39.6	0.88	1.12	11.3	9.3	9.4	5.9	0.4	7.6	2.3	8.7	1.8	67.0	0.9	5.2	4.9	1.1
HLF17 1 III 60‑61	1225.5	12	64	26.4	35.8	0.88	0.83	14.6	6.8	8.7	3.8	1.9	3.7	5.0	5.1	2.6	63.5	1.1	6.0	5.6	1.4
HLF17 1 III 72.5‑73.5	1238	12	56	27.4	33.7	0.90	0.42	12.6	8.0	9.3	4.8	0.7	1.6	5.8	2.8	2.5	67.9	0.9	5.0	4.4	1.2
HLF 17 1 III 82.5‑83	1247.75	11	67	26.9	29.6	0.92	1.78	14.6	6.7	8.7	5.2	3.9	0.4	5.3	2.8	2.7	64.5	0.8	4.2	3.9	1.1
HLF17 1 III 83.5‑84	1248.75	11	56	28.6	45.3	0.93	0.30	17.7	3.0	9.3	7.6	2.2	6.0	4.4	8.7	2.0	63.9	0.7	3.8	3.6	0.9
HLF17 1 III 88.5‑89.5	1254	12	64	27.2	30.5	0.89	1.37	12.9	8.8	9.3	4.4	3.3	6.5	4.8	1.8	2.3	65.7	1.0	5.8	5.0	1.3
HLF17 1 III 95.5‑96.5	1261	13	65	25.9	34.0	0.87	2.50	13.2	7.8	9.0	4.1	3.8	9.3	3.5	8.1	3.5	66.3	1.0	6.2	5.3	1.3
mean		12	64	27.0	34.2	0.89	0.83	14.1	7.0	8.9	6.3	8.3	0.8	7.4	6.4	2.4	65.4	0.9	5.2	4.6	1.2
s.d.		0.1	1.0	1.0	4.7	0.02	0.66	1.8	1.7	1.0	4.1	9.5	4.9	9.7	5.2	1.3	1.8	0.1	0.9	0.7	0.2
T-test (p<0.01)		*	*	*	*	*		*									*		*	*	*

n.m= not measured

882

883

884

Tabel 3. Relative abundance of diatoms in dark and light laminae as counts and biovolume

laminae	depth (cm)		Chaetoceros RS	Chaetoceros dichaeta	Corethron pennatum	Eucampia antarctica	Fragilariopsis curta	Fragilariopsis cylindrus	Fragilariopsis obliquecostata	Rhizosolenia spp.	total	Chaetoceros RS	Chaetoceros dichaeta	Corethron pennatum	Eucampia antarctica	Fragilariopsis curta	Fragilariopsis cylindrus	Fragilariopsis obliquecostata
						relative abudance (counts), %								relative abudance (biovolume), % [a]					
		average biovolume (µm³) [b]										277	19227	70686	40457	642	231	4936	169
light																		
HLF17 1 III 14-15	1179.5	Light	3.6	0.0	17.3	0.0	56.7	2.9	9.2	0.3	90.0	0.1	0.0	89.8	0.0	2.7	0.0	3.3	4.
HLF17 1 III 17-18	1182.5	Light	19.0	0.0	26.1	0.0	19.0	12.5	7.7	0.3	84.5	0.3	0.0	94.7	0.0	0.6	0.1	2.0	2.
HLF 17 1 III 20-21	1185.5	Light	8.2	0.9	5.8	0.0	51.2	3.2	14.3	0.0	83.5	0.4	3.1	77.0	0.0	6.1	0.1	13.2	0.
HLF17 1 III 33-34	1198.5	Light	5.3	0.0	11.3	0.0	45.2	10.7	12.9	0.3	85.6	0.2	0.0	84.4	0.0	3.1	0.3	6.7	5.
HLF17 1 III 34.5-35	1200	Light	7.0	1.0	8.2	0.3	33.4	5.1	14.3	0.5	69.9	0.2	2.5	73.1	1.3	2.7	0.1	8.9	11
HLF 17 1 III 46-47	1211.5	Light	4.5	0.0	36.7	0.0	22.3	7.3	12.3	0.6	83.8	0.0	0.0	93.5	0.0	0.5	0.1	2.2	3.
HLF 17 1 III 51-52	1216.5	Light	7.4	0.8	10.8	0.0	56.8	4.0	6.7	0.0	86.6	0.2	1.8	89.6	0.0	4.3	0.1	3.9	0.
HLF17 1 III 57-58	1222.5	Light	9.5	0.0	20.3	0.0	36.1	6.3	11.0	0.3	83.6	0.2	0.0	91.6	0.0	1.5	0.1	3.5	3.
HLF 17 1 III 63-64	1228.5	Light	8.3	4.3	5.5	0.2	40.1	6.0	12.1	0.0	76.3	0.4	14.5	68.7	1.1	4.5	0.2	10.5	0.
HLF17 1 III 71-72	1236.5	Light	9.4	0.3	16.8	0.1	45.3	2.8	9.3	0.0	84.0	0.2	0.4	93.0	0.5	2.3	0.1	3.6	0.
HLF17 1 III 73.5-74.5	1239	Light	17.4	0.0	9.0	0.2	25.0	3.3	18.2	0.0	73.1	0.6	0.0	84.2	0.9	2.1	0.1	12.0	0.
HLF17 1 III 80.5-81.5	1246	Light	1.3	0.0	44.6	0.0	24.2	2.1	10.5	0.5	82.7	0.0	0.0	97.9	0.0	0.5	0.0	1.6	0.
HLF17 1 III 84-5-85.5	1250	Light	12.5	2.5	14.0	0.0	31.6	6.4	11.4	0.0	78.3	0.3	4.3	88.4	0.0	1.8	0.1	5.0	0.
HLF 1 1 III 86.5-87.5	1252	Light	14.7	0.3	8.3	0.0	24.9	13.4	8.6	0.7	70.8	0.5	0.8	76.1	0.0	2.1	0.4	5.5	14
HLF17 1 III 91-92	1256.5	Light	10.5	1.9	18.6	0.0	35.8	1.9	9.6	0.3	78.6	0.2	2.4	89.0	0.0	1.6	0.0	3.2	3.
		average	**9.2**	**0.8**	**16.9**	**0.0**	**36.5**	**5.9**	**11.2**	**0.2**		**0.3**	**2.0**	**86.1**	**0.3**	**2.4**	**0.1**	**5.7**	**3.**
		s.d.	**5.0**	**1.2**	**11.4**	**0.1**	**12.4**	**3.7**	**3.0**	**0.2**		**0.2**	**3.7**	**8.7**	**0.5**	**1.6**	**0.1**	**3.8**	**4.**
dark																		
HLF17 1 III 1-2	1166.5	Dark	3.0	7.7	0.8	0.0	48.4	3.4	19.9	0.0	83.2	0.2	43.8	17.6	0.0	9.2	0.2	29.0	0.
HLF17 1 III 3-4	1168.5	Dark	8.0	2.6	1.0	0.0	41.6	3.9	18.4	0.4	75.9	0.7	15.9	21.9	0.0	8.6	0.3	29.4	23
HLF17 1 III 6-7	1171.5	Dark	2.4	1.8	0.0	0.0	72.2	2.5	9.1	0.0	87.9	0.5	27.1	0.0	0.0	36.6	0.5	35.4	0.
HLF17 1 III 11-12	1176.5	Dark	4.9	0.0	6.4	0.0	46.0	4.5	23.0	0.0	84.7	0.2	0.0	75.5	0.0	5.0	0.2	19.1	0.
HLF 17 1 III 16-17	1181.5	Dark	3.9	0.9	3.6	0.0	51.3	2.2	22.4	0.5	84.8	0.2	3.3	50.7	0.0	6.6	0.1	22.2	16
HLF 18 1 III 18-19	1183.5	Dark	5.2	1.6	1.3	0.0	39.0	27.2	9.0	0.2	83.6	0.6	13.2	38.0	0.0	10.4	2.6	18.6	16
HLF17 1 III 27-28	1192.5	Dark	9.7	2.1	3.4	0.0	52.3	4.1	17.6	0.0	89.2	0.7	10.0	59.5	0.0	8.3	0.2	21.4	0.
HLF17 1 III 39-40	1204.5	Dark	4.7	0.5	9.3	0.1	18.9	40.4	3.7	0.3	77.9	0.2	1.4	86.4	0.7	1.6	1.2	2.4	6.
HLF17 1 III 42.5-43.5	1208	Dark	11.1	0.2	4.9	0.3	41.6	4.7	18.5	0.2	81.5	0.6	0.7	67.5	2.1	5.2	0.2	17.8	5.
HLF17 1 III 43.5-44	1208.8	Dark	4.3	0.3	19.2	0.1	27.9	1.0	17.8	0.3	70.9	0.1	0.3	89.5	0.3	1.2	0.0	5.8	2.
HLF17 1 III 44.5-45	1209.8	Dark	2.6	0.0	36.3	0.6	25.0	5.9	14.1	0.0	84.5	0.0	0.0	95.8	1.0	0.6	0.1	2.6	0.
HLF17 1 III 48-49	1213.5	Dark	4.2	1.7	15.7	1.7	26.6	9.9	19.3	0.3	79.3	0.1	2.3	80.9	4.9	1.2	0.2	6.9	3.
HLF17 1 III 55-56	1220.5	Dark	5.9	1.4	0.4	0.0	57.6	2.3	18.7	0.5	86.9	0.6	9.8	11.2	0.0	13.2	0.2	32.8	32
HLF17 1 III 60-61	1225.5	Dark	3.8	5.0	1.9	0.0	53.7	5.5	15.1	0.0	84.6	0.3	28.1	39.4	0.0	10.1	0.3	21.8	0.
HLF17 1 III 72.5-73.5	1238	Dark	4.8	2.2	10.7	1.1	41.6	5.8	12.8	0.3	79.2	0.1	4.4	76.7	4.6	2.7	0.1	6.4	4.
HLF 17 1 III 82.5-83	1247.8	Dark	5.2	0.5	13.9	0.8	20.4	5.3	22.8	0.5	69.4	0.1	0.8	79.2	2.5	1.1	0.1	9.1	7.
HLF17 1 III 83.5-84	1248.8	Dark	17.6	0.4	22.2	0.0	16.0	4.4	18.7	0.0	79.3	0.3	0.5	93.1	0.0	0.6	0.1	5.5	0.
HLF17 1 III 88.5-89.5	1254	Dark	14.4	1.0	3.3	0.0	46.5	4.8	11.8	0.5	82.3	0.9	4.5	54.0	0.0	6.9	0.3	13.5	19
HLF17 1 III 95.5-96.5	1261	Dark	4.1	3.5	3.8	0.3	49.3	3.5	18.1	0.6	83.3	0.2	11.6	46.5	2.2	5.5	0.1	15.4	18
		average	**6.3**	**1.8**	**8.3**	**0.3**	**40.8**	**7.4**	**16.4**	**0.2**		**0.4**	**9.3**	**57.0**	**1.0**	**7.1**	**0.4**	**16.6**	**8.**
		s.d.	**4.1**	**1.9**	**9.5**	**0.5**	**14.9**	**9.7**	**5.2**	**0.2**		**0.3**	**12.0**	**29.4**	**1.6**	**8.1**	**0.6**	**10.3**	**9.**
T-test ($p<0.05$)					*									*		*		*
T-test ($p<0.01$)								*						*			*	

[a] Percent biovolume $=100*$ (% relative abundance $*$ V avg) / Total biovolume (from Alley et al., 2018)

[b] average biovolume from Alley et al., 2018

885